Garnet and scheelite chemistry of the Weijia tungsten deposit, South China: Implications for fluid evolution and W skarn mineralization in F-rich ore system

Xu-Dong Huang, Jian-Jun Lu, Rong-Qing Zhang, Stanislas Sizaret, Dong-Sheng Ma, Ru-Cheng Wang, Xian Zhu, Zhong-Yuan He

Journal Pre-proofs

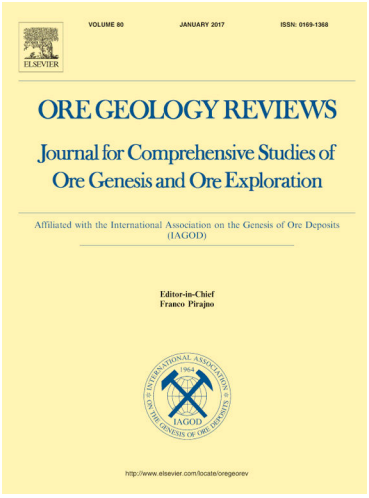

Garnet and scheelite chemistry of the Weijia tungsten deposit, South China: Implications for fluid evolution and W skarn mineralization in F-rich ore system

Xu-Dong Huang, Jian-Jun Lu, Rong-Qing Zhang, Stanislas Sizaret, Dong-Sheng Ma, Ru-Cheng Wang, Xian Zhu, Zhong-Yuan He

PII: S0169-1368(22)00037-3
DOI: https://doi.org/10.1016/j.oregeorev.2022.104729
Reference: OREGEO 104729

To appear in: *Ore Geology Reviews*

Received Date: 25 December 2021
Revised Date: 18 January 2022
Accepted Date: 24 January 2022

Please cite this article as: X-D. Huang, J-J. Lu, R-Q. Zhang, S. Sizaret, D-S. Ma, R-C. Wang, X. Zhu, Z-Y. He, Garnet and scheelite chemistry of the Weijia tungsten deposit, South China: Implications for fluid evolution and W skarn mineralization in F-rich ore system, *Ore Geology Reviews* (2022), doi: https://doi.org/10.1016/j.oregeorev.2022.104729

Garnet and scheelite chemistry of the Weijia tungsten deposit, South China: Implications for fluid evolution and W skarn mineralization in F-rich ore system

Xu-Dong Huang[a], Jian-Jun Lu[a,*], Rong-Qing Zhang[a], Stanislas Sizaret[b], Dong-Sheng Ma[a], Ru-Cheng Wang[a], Xian Zhu[c], Zhong-Yuan He[d]

[a] State Key Laboratory for Mineral Deposits Research, Frontiers Science Center for Critical Earth Material Cycling, Institute of Continental Geodynamics, School of Earth Sciences and Engineering, Nanjing University, Nanjing 210023, China

[b] Institut des Sciences de la Terre d'Orléans, UMR 7327-CNRS/Université d'Orléans/BRGM, Orléans 45071, France

[c] Team 418 of Hunan Bureau of Geology and Mineral Exploration and Development, Loudi 417000, China

[d] First Team of Hunan Nonferrous Metals Geological Exploration Bureau, Chenzhou 423000, China

[*] Corresponding author. E-mail address: lujj@nju.edu.cn (J.-J. Lu).

Abstract

Fluid evolution is an essential subject in the studies of hydrothermal ore-forming processes. Garnet and scheelite prevail in W-bearing skarn deposits and record plentiful information on W skarn mineralization. In-situ LA-ICP-MS trace element analyses have been carried out on the garnet and scheelite from the F-rich Weijia W deposit in South China to constrain the processes of fluid evolution and W skarn mineralization. The Weijia W deposit mainly consists of calcic and magnesian skarns and was formed through six stages of alteration and mineralization. Two stages of fluid exsolution are recognized in the magmatic-hydrothermal system. The earlier exsolved fluids are Cl-rich with rightward-sloping REE patterns and result in pre-ore

skarnization. The later exsolved fluids are F-rich with relatively flat REE patterns and are responsible for W mineralization. The pre-ore garnets are LREE-enriched and HREE-depleted whereas the syn-ore garnets are LREE-depleted and HREE-enriched with lower δEu values than the former, denoting a transition from wall rock-controlled to magmatic fluid-dominated fluid-rock interaction. Combined with the skarn occurrences, mineral assemblages, and garnet textures, it is revealed that the mechanism of skarn formation shifts from more diffusive metasomatism under lower water/rock ratios to more advective metasomatism at higher water/rock ratios. The advective metasomatism with a high flux of ore-forming fluids is hydrodynamically favorable for the consequent W mineralization. The earliest-formed scheelite is akin to the host granite porphyry in REE patterns and can reflect the features of initial mineralizing fluids. It has high ΣREE (1255–5059 ppm), Y (616–1416 ppm), Nb (585–2629 ppm), Ta (14–248 ppm), Mn (up to 1977 ppm) and low Mo (mostly < 1000 ppm) contents, indicating that the primary F-rich magmatic fluids are reduced and enriched in REEs, Y, Nb, and Ta. The contents of ΣREE, Y, Nb, and Ta in scheelite are decreasing with the evolution of the F-rich mineralizing fluids. The latest-formed scheelites have distinctly lower ΣREE (2.9–140 ppm), Y (0.01–4.1 ppm), Nb (1.7–77 ppm), and Ta (0.04–0.19 ppm) contents and higher $(La/Yb)_N$ ratios and δEu values. They show 1:1 positive correlation of Eu_N vs. Eu* N and have high Mo (up to 129466 ppm) and low Mn (as low as 3.4 ppm) contents, implying involvement of meteoric waters in the evolved ore-forming fluids and an oxidizing condition. Fluid-rock interaction, mineral precipitation, and fluid mixing largely control the process of fluid evolution. Fluorine consumption due to the formation of fluorite and the other F-rich minerals is vital for the compositional evolution of F-rich mineralizing fluids. The decrease of F concentration in fluids will depress the solubilities of REEs, Y, Nb, and Ta and enhance the LREE/HREE fractionation. Greisenization and skarnization induced the neutralization of the acidic W-bearing fluids and the

liberation of Ca from the granite porphyry and carbonate strata and then triggered the scheelite precipitation. The carbonate strata contain abundant Ca and the granite porphyry is poor in Ca, and thus the economic W mineralization dominantly occurs in the skarns.

Keywords: F-rich ore system, fluid exsolution, fluid-rock interaction, metasomatism mechanism, fluid evolution, scheelite precipitation

1. Introduction

The compositions and physicochemical conditions of hydrothermal fluids exsolved from crystallizing magmas have a crucial effect on fluid-melt element partitioning and subsequent ore-forming processes (Hedenquist and Lowenstern, 1994; Heinrich and Candela, 2014). Large tungsten deposits are dominantly related to highly fractionated F-rich granites (Černý et al., 2005; Wang et al., 2021). Skarn is one of the most important types of W mineralization (Einaudi et al., 1981; Meinert et al., 2005). Aksyuk (2000) quantitatively evaluated the fluid F activities of various mineralized skarn systems by biotite and phlogopite fluorimeters and proved that the F-enriched signature is typical of rare metal leucogranites, Li-F granites and pegmatites, and related W, Be, U, Th, rare earth element (REE), Ta, Nb, Li, and Sn skarn deposits. The widespread W skarn deposits in South China (Zhao et al., 2017; Mao et al., 2019) provide excellent examples for studying the characteristics and evolution of magmatic fluids in F-rich ore systems.

The trace element compositions of ore and gangue minerals from hydrothermal deposits preserve abundant vestiges of ore-forming processes and are powerful tools to decipher the origin and evolution of mineralizing fluids (e.g., Song et al., 2014; Sun and Chen, 2017; Legros et al., 2018; Xiao et al., 2018; Zhang et al., 2018; Chen et al., 2020a; Xu et al., 2020). Especially, the application of in-situ laser ablation-inductively coupled plasma-mass spectrometry (LA-ICP-MS)

analytical technique combined with backscattered electron (BSE) and/or cathodoluminescence (CL) imaging provide us with a more detailed view into the ore-forming processes (e.g., Ding et al., 2018; Li et al., 2018; Zhao et al., 2018; Park et al., 2019; Tian et al., 2019; Han et al., 2020; Carocci et al., 2021).

Garnet and scheelite are common in W-bearing skarn deposits. Garnet is mostly isometrical with a general chemical formula of $X_3Y_2Z_3O_{12}$, where X, Y, and Z successively refer to divalent cations (Ca, Mg, Mn, or Fe^{2+}) in dodecahedral site, trivalent cations (Fe^{3+}, Al, and Cr) in octahedral site, and dominantly Si in tetrahedral site (Gaspar et al., 2008; Grew et al., 2013). Scheelite ($CaWO_4$) has a tetragonally symmetric crystal structure constructed by tetrahedral $[WO_4]^{2-}$ groups and irregular dodecahedral $[CaO_8]^{14-}$ groups (Ghaderi et al., 1999; Brugger et al., 2000). Considerable amounts of trace elements, such as REEs, Y, Sr, and Na, can substitute for Ca in both of them on account of the comparable ionic radii and valencies (Ghaderi et al., 1999; Gaspar et al., 2008). Likewise, substantial Mo and Nb can be incorporated into scheelite by occupying the position of W (e.g., Zhao et al., 2018; Li et al., 2019). The trace element variations of scheelite and garnet are largely controlled by the substitution mechanisms, the sources, compositions and physicochemical conditions of associated fluids, the dynamics of hydrothermal system (including fluid-rock interaction and mineral precipitation), and the kinetics of mineral growth (Ghaderi et al., 1999; Brugger et al., 2000; Smith et al., 2004; Gaspar et al., 2008).

The Weijia W deposit in the Nanling Range of South China is a recently discovered large scheelite skarn deposit that comprises primary magnesian W skarn (240 kt WO_3 at 0.18 wt%) and subordinate calcic W skarn (60 kt WO_3 at 0.24 wt%). It is genetically linked to highly fractionated granite porphyry (Zhao et al., 2016; Huang et al., 2017) and is characterized by extreme enrichment of fluorine with general CaF_2 grades of 5–18 wt%. In this publication, we present a combined study on garnet and scheelite mineralogy of the Weijia W skarn deposit,

including textures as well as in-situ trace element compositions, aiming to reveal the processes of fluid evolution and W skarn mineralization in a F-rich ore system. Our achievements highlight the significance of mineral trace element geochemistry in elucidating complex ore-forming processes.

2. Geological setting

South China is the most important W metallogenic province around the world and holds the world's largest W production (Zhao et al., 2017; Mao et al., 2019). The Yangtze and Cathaysia Blocks were amalgamated together along the Jiangnan Orogen into a unified South China Block (Fig. 1a) during Neoproterozoic (Wang et al., 2007). Since then, South China has undergone Neoproterozoic, Silurian, Triassic, Jurassic, and Cretaceous tectonic-magmatic events and associated W-Sn mineralization (Chen et al., 2013; Mao et al., 2013, 2019; Shu et al., 2015; Zhang et al., 2019). The stable neritic-bathyal clastic deposition from Neoproterozoic to Ordovician and littoral-neritic carbonate deposition from Devonian to Triassic were responsible for the formation of regionally important ore-hosting strata for subsequent Mesozoic mineral deposits. Most W-Sn deposits in South China were formed during Late Mesozoic and are genetically closely related to contemporaneous granites (Chen et al., 2013; Mao et al., 2013, 2019; Zhao et al., 2017). The Late Mesozoic explosive granitic magmatism and concomitant W-Sn mineralization were geodynamically linked to the subduction and roll-back of paleo-Pacific plate which induced asthenosphere upwelling and basaltic magma underplating (Zhou and Li, 2000; Li and Li, 2007). It is widely accepted that the underplated basaltic magmas provided the necessary heat to trigger extensive crustal melting and generation of voluminous felsic magmas (Zhou and Li, 2000; Zhou et al., 2006).

The Nanling Range situated in the central Cathaysia Block (Fig. 1a) is one of the 21 key metallogenic belts in China. It possesses numerous W-Sn deposits that were predominantly

formed in Late Jurassic (Mao et al., 2007, 2013, 2019). The W-bearing granites are generally multi-facies mainly consisting of biotite, two-mica, and muscovite granites, which show evident highly fractionated features (Chen et al., 2008; Zhang et al., 2017). Wolframite quartz vein and greisen and scheelite skarn constitute the majority of W deposits in the Nanling Range (Chen et al., 2008; Zhao et al., 2017; Mao et al., 2019). Topaz and fluorite are frequently observed in these W deposits, indicating F-rich magmatic-hydrothermal environments (e.g., Legros et al., 2018; Chen et al., 2020a). Wall-rock compositions apparently control the styles of W mineralization. The wolframite quartz vein and greisen deposits occur principally in the eastern Nanling Range where the strata are dominated by Neoproterozoic to Ordovician clastic metasedimentary rocks (e.g., Xihuashan, Piaotang, and Maoping, Mao et al., 2007), while the scheelite skarn deposits are largely distributed in the western Nanling Range where the Devonian to Triassic carbonate strata are well developed (e.g., Xintianling, Shizhuyuan, and Yaogangxian, Mao et al., 2007). The Weijia W deposit is one of these scheelite skarn deposits (Fig. 1a). Huang et al. (2017) reported a zircon U-Pb age of 158.3±2.2 Ma for the Weijia granite porphyry. Molybdenite Re-Os dating revealed that this deposit was formed at 159.0±5.6 Ma (Zhao et al., 2016), manifesting a genetic linkage between the Weijia W skarn deposit and granite porphyry.

3. Deposit geology

The exposed strata in the Weijia W skarn deposit are mainly Middle–Late Devonian carbonate rocks that include the Middle Devonian Qiziqiao Formation and Upper Devonian Shetianqiao and Xikuangshan Formations (Fig. 1b). The Qiziqiao Formation is composed of a lower member of limestone, a middle member of dolostone with intercalated dolomitic limestone, and an upper member of limestone locally with intercalated dolomitic limestone and lenticular dolostone (Figs. 1b and 2). Both the Shetianqiao and Xikuangshan Formations principally

144 comprise limestone and dolomitic limestone. These carbonate strata are slightly folded and
145 broadly strike NNW–SSE and dip 5–35° to SWW (Figs. 1b and 2).

146 The magmatic rocks associated with the Weijia W skarn deposit are granite porphyry which
147 was dominantly emplaced as scattered bosses, ductoliths, and dykes, with a total exposure area of
148 ca. 1.3 km^2 (Figs. 1b and 2). The granite porphyry has light red to off-white color and shows a
149 typical subvolcanic porphyritic texture (Figs. 3a and 4a). It contains 30–50 vol% of fine- to
150 medium-grained phenocrysts and 50–70 vol% of felsitic to fine-grained matrix. Rock-forming
151 minerals are K-feldspar (ca. 37 vol%), quartz (ca. 35 vol%), albite (ca. 25 vol%, An < 5), and
152 minor muscovite (ca. 2 vol%) and biotite (ca. 1 vol%). The majority of phenocrysts consist of
153 quartz, K-feldspar, albite, and biotite (Fig. 4a) and muscovite mostly occurs in the matrix (Fig.
154 4b). Accessory minerals include zircon, thorite, apatite, ilmenite, rutile, fluorite, scheelite,
155 monazite, xenotime, niobite, samarskite, fergusonite, and parisite.

156 At the apex of the Weijia granite porphyry, there are some late-magmatic to hydrothermal
157 veins with a vertically upward zonation from K-feldspar-quartz pegmatite veins and
158 (K-feldspar)-quartz veins to stockwork quartz veinlets (Fig. 3b) (Huang, 2018). The stockwork
159 quartz veinlets contain fluorite and muscovite and are associated with weak greisenization that
160 occurs as interstitial muscovite and muscovite-fluorite aggregates in the granite matrix (Fig. 4b).
161 They contain a few scheelite grains (Fig. 4c) but are of no economic significance. Economic
162 calcic and magnesian W skarns are distributed along the contact zones between the granite
163 porphyry and the upper and middle members of the Qiziqiao Formation, respectively (Fig. 2).
164 The former is developed as massive at depth shallower than 300 m and is partially exposed on the
165 surface, while the latter is stratiform with buried depth of 200–900 m (Fig. 2). The calcic skarn is
166 characterized by earlier disseminated garnet (yellow-brown) and pyroxene (light-green) and later
167 stockwork garnet (red-brown) followed by stockwork pyroxene (dark-green) (Fig. 3c and d).

Scheelite mostly intimately coexists with the stockwork garnet and pyroxene (Fig. 5a–d). The magnesian skarn generally appears as green-colored stockwork veinlets in the fissures of dolostone and primarily comprises phlogopite and serpentine (Fig. 3e and f) occasionally with a few earlier garnet and pyroxene. Scheelite dominantly occurs within the stockwork magnesian skarn veinlets (Fig. 5e–g).

We have detailedly investigated the petrographic relationships, mineral assemblages, and the textures and compositions of garnets and scheelites, and thus six stages of alteration and mineralization are established in the Weijia W skarn deposit. The pre-ore stage 1 is characterized by disseminated and stockwork skarnization in the limestone and dolostone, respectively (Fig. 3c–f). In this stage, the calcic skarn developed garnet (Grt_C 1), pyroxene (Px_C 1), and magnetite (Fig. 5a) and the magnesian skarn generated garnet (Grt_M 1), pyroxene (Px_M 1), and marialite ($Na_4Al_3Si_9O_{24}Cl$, Fig. 5h). The Grt_C 1 encloses the Px_C 1 and is replaced by fluorite (Fig. 5b). The stockwork quartz veinlets associated with weak greisenization were formed during the stage 2 within the granite porphyry (Fig. 3b). The minerals in the stockwork quartz veinlets include quartz, fluorite, muscovite, and a few scheelite grains (Sch_Q 2) (Fig. 4c). In the stage 3, the calcic skarn is dominated by wollastonite, stockwork garnet (Grt_C 3), scheelite (Sch_C 3), vesuvianite, and fluorite (Figs. 3c–d and 5c) and the stockwork magnesian skarn by garnet (Grt_M 3), scheelite (Sch_M 3), chondrodite, and fluorite (Fig. 5e). The stage 4 is developed as stockwork pyroxene (Px_C 4), scheelite (Sch_C 4), and fluorite with minor chlorite in the calcic skarn (Figs. 3c–d and 5d) and chlorite, sericite, and calcite in the adjacent granite porphyry. In this stage, the stockwork magnesian skarn in the dolostone is featured by the formation of phlogopite, serpentine, scheelite (Sch_M 4), and fluorite with a few sellaite, talc, and chlorite (Figs. 3e–f and 5e–h) and the adjacent granite porphyry was altered by serpentine, phlogopite, sericite, and calcite with scheelite mineralization. Sporadically disseminated pyrite, pyrrhotite, arsenopyrite, chalcopyrite,

192 sphalerite, and galena were formed during the stage 5 and overprint the earlier skarn minerals
193 (Huang, 2018). The post-ore stage 6 is presented as barren (K-feldspar)-quartz, fluorite, and
194 calcite veinlets cutting the earlier skarn and sulfide minerals (Fig. 3c–f).

195 **4. Sampling and analytical methods**

196 **4.1. Sample collection**

197 We have systematically collected the samples of the granite porphyry and its stockwork
198 quartz veinlets, calcic skarn, and magnesian skarn from surface outcrops and drill cores in the
199 Weijia W deposit. The drill core locations and sampling depths are shown in Fig. 1b and listed in
200 Supplementary Tables S1–S4, respectively. These samples were prepared as polished thin
201 sections firstly for petrographic and mineral textural studies and then for mineral compositional
202 analyses.

203 **4.2. BSE and CL imaging**

204 BSE imaging of garnet and scheelite was conducted through a ZEISS MERLIN Compact
205 scanning electron microscope (SEM) equipped with a Bruker XFlash 6 | 30 silicon drift detector
206 at Institut des Sciences de la Terre d'Orléans (ISTO), France. The analytical conditions included
207 an accelerating voltage of 15 kV, a current up to 100 nA with resolution up to 0.8 nm, and a
208 working distance of 10 mm.

209 CL imaging of scheelite was performed by a TESCAN MIRA 3 LMH field emission SEM
210 equipped with a TESCAN A75c CL detector at Nanjing Hongchuang Geological Exploration
211 Technology Service Co., Ltd., China. The analytical conditions included an accelerating voltage
212 of 7 kV, an emission current of 0.15 mA and a specimen current of 2 nA, and a working distance
213 of 18–19 mm.

214 **4.3. Electron microprobe analyses**

Major element analyses of garnet and pyroxene were accomplished by a CAMECA SX50 electron microprobe at ISTO, France. The operating conditions included an accelerating voltage of 15 kV, a beam current of 10 nA with diameter of 1 μm, and counting times of 10 s for each element and 5 s for background. Natural albite (Si$K\alpha$ and Na$K\alpha$), andradite (Ca$K\alpha$), orthoclase (K$K\alpha$), and topaz (F$K\alpha$) and synthetic $MnTiO_3$ (Ti$K\alpha$ and Mn$K\alpha$), Al_2O_3 (Al$K\alpha$), Fe_2O_3 (Fe$K\alpha$), and MgO (Mg$K\alpha$) were used as standards. The detection limits are better than 0.1 wt% for Si, Al, Mg, Ca, and Na, 0.15 wt% for Ti and K, 0.3 wt% for Mn, 0.35 wt% for Fe, and 0.5 wt% for F. All data were corrected with standard ZAF correction procedures.

4.4. In-situ LA-ICP-MS analyses

In-situ trace element analyses of garnet and scheelite were carried out through an Agilent 7700× ICP-MS coupled to an Excite 193 nm Photon Machines laser ablation system at Nanjing FocuMS Technology Co., Ltd., China. Helium gas was used as the carrier to efficiently transport aerosol and mix with argon gas via a T-connector before entering the ICP-MS. The instrument settings were optimized by ablating the NIST SRM 610 synthetic glass to obtain maximum signal intensities and keeping low ThO/Th ratios (< 0.3%) to reduce the oxide and doubly charged ion interferences. Each sample analysis was conducted by a 25–50-μm ablating spot at 5–8 Hz repetition rate with fluence of 6.06 J/cm^2 for 40 s after measuring the gas blank for 15 s. After every 8–10 sample analyses, the external standards (garnet: NIST SRM 612, 610 and USGS BIR-1G, BHVO-2G, BCR-2G; scheelite: NIST SRM 612, 610) were measured once to correct the time-dependent sensitivity drift and mass discrimination. The off-line data processing was performed by the ICPMSDataCal software using 100%-normalization strategy without applying an internal standard (Liu et al., 2008).

5. Results

5.1. Garnet and scheelite textures

The disseminated Grt_C 1 usually has millimeter-scale grain sizes and is euhedral to subhedral and oscillatorily zoned with the band width of a dozen to dozens of microns (Figs. 5a–b and 6a), while the stockwork Grt_C 3 is anhedral without obvious zonation (Figs. 5c and 6a–b). The Grt_C 3 cuts the Grt_C 1 (Fig. 6a) and coexists with the Sch_C 3 (Fig. 6b). The Grt_M 1 is coarser, subhedral, and relatively homogeneous whereas the Grt_M 3 is finer, anhedral, and distinctly heterogeneous (Fig. 6c–e). The Grt_M 3 replaces the Grt_M 1 (Fig. 6c) and coexists with the Sch_M 3 (Fig. 6d and e). In light of the BSE images, both the Grt_M 1 and Grt_M 3 can be subdivided into two subgenerations, i.e., the darker Grt_M 1A and Grt_M 3A and the brighter Grt_M 1B and Grt_M 3B (Fig. 6d–f). The Grt_M 1A shows micron-scale oscillatory zonation whereas the other three subgenerations do not (Fig. 6d–f). The boundary between the Grt_M 3A and Grt_M 3B is rather chaotic (Fig. 6f).

The Weijia scheelite grains are mostly 50–400 μm in size (Figs. 5 and 7). They are generally anhedral (Figs. 5 and 7) and some of the earliest-formed ones (Sch_Q 2) are subhedral (Fig. 7a). The Sch_Q 2 coexists with molybdenite and is oscillatorily zoned with the band width of several to a dozen microns (Fig. 7a). The Sch_C 3 and Sch_M 3 show conspicuous micron-scale oscillatory zonation, while the Sch_C 4 and Sch_M 4 are relatively homogeneous (Fig. 7b–g). The Sch_C 4 cuts the Sch_C 3 in the stockwork garnet veinlets (Fig. 7b and c) and the Sch_M 4 replaces the Sch_M 3 (Fig. 7f).

5.2. Garnet and pyroxene major elements

The in-situ major and trace element analytical results of different generations of garnets, pyroxenes, and scheelites from the Weijia W skarn deposit are listed in Supplementary Tables S1–S4. The Grt_C 1 has andraditic compositions ($Grs_{1–14}Adr_{81–93}$), while the Grt_C 3 belongs to intermediate grandite ($Grs_{38–63}Adr_{33–57}$) (Fig. 8a). Both the Grt_M 1 and Grt_M 3 are grossularitic garnet ($Grs_{67–84}Adr_{10–22}$, Fig. 8b) and contain more MgO (mostly 1.5–2.6 wt%) than the Grt_C 1

and Grt_C 3 (< 0.54 wt%) (Table S1). These garnets are F-bearing. In the same stage, the garnet in the magnesian skarn is richer in F (Grt_M 1: 0.51–2.8 wt%; Grt_M 3: 2.7–4.1 wt%) than that in the calcic skarn (Grt_C 1: < 0.77 wt%; Grt_C 3: < 1.4 wt%) (Table S1). The stage-3 garnet has higher F contents than the stage-1 garnet whether in the calcic or magnesian skarn (Table S1). The Px_C 1 is diopsidic pyroxene ($Di_{68–99}Hd_{0–27}$) whereas the Px_C 4 has hedenbergitic compositions ($Di_{0–16}Hd_{78–95}$) (Fig. 8c). The Px_M 1 is almost pure diopside ($Di_{98–100}Hd_0$, Fig. 8d).

5.3. Garnet trace element compositions

The Grt_C 1 shows slightly rightward-sloping chondrite-normalized REE patterns without obvious Eu anomalies (Fig. 9a), while the Grt_C 3 exhibits light REE (LREE)-depleted [$(La/Sm)_N$ = 0.05–0.16] and heavy REE (HREE)-enriched REE patterns with apparent Eu negative anomalies (δEu = 0.12–0.21) (Figs. 9b and 10a). The Grt_M 1 displays LREE-enriched and HREE- and Eu-depleted REE patterns whereas the Grt_M 3 is significantly richer in HREEs and more depleted in Eu than the former (Fig. 9c and d). The Grt_M 1B has higher REE (especially LREE) contents and stronger Eu negative anomalies than the Grt_M 1A (Fig. 9c). The Grt_M 3A presents relatively flat and strongly Eu-depleted (δEu = 0.007–0.02) REE patterns and the Grt_M 3B is distinguished from the former by striking depletions of LREEs [$(La/Sm)_N$ = 0.001–0.005] (Figs. 9d and 10a). Notably, all the REE patterns of the Grt_M 1 and Grt_M 3 are Tm-Yb-Lu-upwarped (Fig. 9c and d).

The Grt_C 1 and Grt_C 3 have higher Ti, V, Cr and lower Na, Zn, Sr contents than the Grt_M 1 and Grt_M 3 on the whole (Table S3). The Grt_C 1 contains more W (7.1–1181 ppm) and less Nb (0.25–8.6 ppm) than the Grt_C 3 (5.6–168 ppm W, 2.3–21 ppm Nb) (Table S3). The Grt_M 1 and Grt_M 3 have comparable W contents (Grt_M 1: 0.42–3.1 ppm; Grt_M 3: 0.40–5.4 ppm) and Nb contents (Grt_M 1: 1.4–74 ppm; Grt_M 3: 6.3–26 ppm) (Table S3). The Ta contents of these garnets are low (0.01–0.42 ppm, Table S3).

5.4. Scheelite trace element compositions

The Sch_Q 2 shows flat chondrite-normalized REE patterns [$(La/Yb)_N$ = 0.29–2.7] with strong Eu negative anomalies (δEu = 0.006–0.06) and contains the highest ΣREE (1255–5059 ppm), Y (616–1416 ppm), Nb (585–2629 ppm), Ta (14–248 ppm) and lowest Mo (mostly < 1000 ppm) contents among all generations of scheelites (Figs. 11a and 12). The Sch_C 3 exhibits slightly rightward-sloping [$(La/Yb)_N$ = 4.0–67] and Eu-depleted (δEu = 0.03–0.36) REE patterns (Figs. 11b and 12a), while the Sch_C 4 is LREE-enriched and HREE-depleted [$(La/Yb)_N$ = 338–4332] with negligible Eu anomalies (δEu = 0.81–2.5) (Figs. 11c and 12a). The Sch_M 3 displays mildly HREE-enriched to HREE-depleted [$(La/Yb)_N$ = 0.07–17] and strongly Eu-depleted (δEu = 0.001–0.13) REE patterns (Figs. 11d and 12a) whereas the Sch_M 4 is enriched in LREEs and depleted in HREEs [$(La/Yb)_N$ = 22–238] with weak Eu anomalies (δEu = 0.58–4.9) (Figs. 11e and 12a). The $(La/Yb)_N$ ratios of the Sch_C 3 and Sch_C 4 are higher than those of the Sch_M 3 and Sch_M 4, respectively (Fig. 12a). The Mg contents of the Sch_C 3 (12–96 ppm) and Sch_C 4 (2.6–13 ppm) are distinctly lower than those of the Sch_M 3 (up to 16729 ppm) and Sch_M 4 (up to 13565 ppm) (Table S4). The Sch_C 4 and Sch_M 4 contain significantly less ΣREE, Y, Nb, and Ta than the Sch_C 3 and Sch_M 3 (Fig. 12b and c). Notably, the scheelite Mn content is negatively correlated to the scheelite Mo content (Fig. 12d).

6. Discussion

6.1. REE substitution mechanisms

The substitution mechanisms of REEs in skarn garnets mainly include (1) $X^{2+} + Si^{4+} = REE^{3+} + Z^{3+}$; (2) $X^{2+} + Y^{3+} = REE^{3+} + Y^{2+}$; (3) $2X^{2+} = REE^{3+} + X^{+}$; and (4) $3X^{2+} = 2REE^{3+} + \square_X$, where X^+, X^{2+}, Y^{2+}, Y^{3+}, Z^{3+} are essentially Na^+, Ca^{2+}, Mg^{2+} or Fe^{2+}, Fe^{3+} or Al^{3+}, Al^{3+}, respectively, and $\square_X$ represents a X-site vacancy (Ismail et al., 2014; Fei et al., 2019; Tian et al.,

2019). There is no correlation between the Na and ΣREE–Eu+Y contents of the Weijia garnets (Table S3), suggesting that the incorporation of REEs did not follow the Eq. (3). The positive ΣREE–Eu+Y vs. Mg correlation of the Grt_C 1 ($Ca^{2+} + Fe^{3+} = REE^{3+} + Mg^{2+}$, Fig. 13a) and negative ΣREE–Eu+Y vs. Al correlation of the Grt_C 3 ($Ca^{2+} + Al^{3+} = REE^{3+} + Fe^{2+}$, Fig. 13b) are indicative of the mechanism (2), i.e., the menzerite-type substitution (Grew et al., 2010). The mechanism (1), i.e., the yttrogarnet (YAG)-type substitution, is common for Al-rich garnets (e.g., Jaffe, 1951; Røhr et al., 2007; Yang et al., 2013) and favors incorporating HREEs. Tm (0.994 Å), Yb (0.985 Å), and Lu (0.977 Å) have almost the ideal REE^{3+} radius (0.99 Å) for this type of substitution (Ding et al., 2018; ionic radii from Shannon, 1976, the same below). The Tm-Yb-Lu-upwarped REE patterns (Fig. 9c and d) and grossularitic compositions (Fig. 8b) of the Grt_M 1 and Grt_M 3 accord with the YAG-type substitution. The $\square_X$-involved substitution mechanism is difficult to evaluate but cannot be absolutely excluded (Gaspar et al., 2008; Fei et al., 2019).

The substitution of REEs into scheelite is dominated by the following three mechanisms: (1) $Ca^{2+} + W^{6+} = REE^{3+} + Nb^{5+}$; (2) $2Ca^{2+} = REE^{3+} + Na^{+}$; (3) $3Ca^{2+} = 2REE^{3+} + \square_{Ca}$, where $\square_{Ca}$ is a Ca-site vacancy (Ghaderi et al., 1999; Song et al., 2014; Sun and Chen, 2017). The correlational plots of Nb+Ta and Na vs. ΣREE–Eu+Y contents (Fig. 14a and b) reveal that the incorporation of REEs into the Sch_Q 2, Sch_C 3, and Sch_M 3 followed principally the Eq. (1) and subordinately the Eq. (2), while the Sch_C 4 and Sch_M 4 accommodated REEs only through the mechanism (1). Both the 1:1 atomic ratios of Nb+Ta+Na to ΣREE–Eu+Y of the Sch_Q 2, Sch_C 3, and Sch_M 3 (Fig. 14c) and Nb+Ta to ΣREE–Eu+Y of the Sch_C 4 and Sch_M 4 (Fig. 14a) preclude the possibility of the $\square_{Ca}$-involved substitution.

6.2. Two-stage fluid exsolution during magmatic evolution

Experiments on the fluid-melt distribution of F and Cl show that F is relatively concentrated in granitic melts and that Cl strongly partitions into aqueous fluids (London et al., 1988; Webster and Holloway, 1988, 1990; Webster, 1992). Therefore, in a F- and Cl-bearing magmatic-hydrothermal system, the Cl-rich fluids tend to exsolve earlier than the F-rich fluids during magmatic evolution. According to the variations of biotite Cl/F ratios and fluorite REE tetrad effects, Berni et al. (2017) recognized an earlier Cl-rich fluid exsolution at the transition from less evolved porphyritic granite to more evolved equigranular granite and a later F-rich fluid exsolution at the stage of equigranular granite and stockscheider pegmatite in the Kymi topaz granite stock, south Finland. Audétat et al. (2000) carried out in-situ compositional analyses of melt and fluid inclusions and Rayleigh fractionation modeling to constrain the late magmatic to early hydrothermal evolution of the Sn-W-F-mineralized Mole granite, eastern Australia. They propounded that in the fractionating Mole granite the earlier exsolved fluids are Cl-rich and more enriched in Sn whereas the later exsolved fluids are F-rich and more enriched in W.

The occurrence of abundant fluorite and the other F-rich minerals including sellaite, garnet (Table S1), vesuvianite, phlogopite (Table S6), and serpentine in the Weijia W skarn deposit (Huang, 2018) evidently demonstrates that the ore-forming fluids are F-enriched and were exsolved from F-rich granitic magmas. To quantitatively evaluate the F activities of ore-forming fluids, the compositions of biotite in the Weijia granite porphyry are used to calculate the fluid HF concentrations by the biotite fluorimeter of Aksyuk (2000). There are two types of biotites in the granite porphyry, one is relatively fresh (Fig. 4a) and the other is altered (Fig. 4d). The fresh biotite has F contents of 2.42–4.84 wt% (Table S6) and yields fluid HF concentrations of $10^{-1.3}$ to $10^{-1.0}$ mol/L that are comparable to those of the F-rich Aqshatau and Qysylrai leucogranites, Central Kazakhstan (Aksyuk, 2000). The F contents of the altered biotite are 0.32–1.95 wt%

(Table S6) and the corresponding fluid HF concentrations are $10^{-2.3}$ to $10^{-1.5}$ mol/L which resemble those of the F-rich Grenvillian pegmatites, Canada (Aksyuk, 2000).

Fluorine will dramatically reduce the viscosity and minimum liquidus temperature of silicate melts (Manning, 1981; Dingwell et al., 1985) and protract the process of fractional crystallization and then facilitate W enrichment in the residual melts (Keppler and Wyllie, 1991; Audétat et al., 2000). The Weijia granite porphyry exhibits obvious variations of major and trace element compositions, for example, the Mg/(Mg+Fe) ratio varies from 0.07 to 0.64 and the Rb/Sr ratio varies from 8.8 to 22.4 (Fig. 15). The increasing Rb/Sr ratio with decreasing Mg/(Mg+Fe) ratio denotes a magmatic evolutionary trend and manifests that the Weijia granite porphyry is a fractionated granite (Fig. 15).

The replacement of the Grt_C 1 and Px_C 1 by fluorite (Fig. 5b) suggests that the stage-1 skarn minerals were formed earlier than the influx of F-rich magmatic-hydrothermal fluids. Whether in the calcic or magnesian skarn, the stage-1 garnet contains less F than the stage-3 garnet (Table S1), implying relatively F-poor compositions of the stage-1 fluids. Significantly, the occurrence of Cl-rich marialite in the stage-1 magnesian skarn (Fig. 5h) indicates that the stage-1 fluids are probably Cl-rich. Analyses of trace elements in fluid inclusions have revealed that the Cl-rich magmatic-hydrothermal fluids are normally LREE-enriched and HREE-depleted with negative Eu anomalies (e.g., Norman et al., 1989; Ghazi et al., 1993; Banks et al., 1994). The Grt_M 1 shows rightward-sloping and Eu-depleted REE patterns and has distinctly higher LREE/HREE ratios than both the granite porphyry and host dolostone (Fig. 9c), supporting that the stage-1 skarnization was induced by the input of Cl-rich hydrothermal fluids which were exsolved earlier than the F-rich hydrothermal fluids from the evolved granitic magmas.

The REE characteristics of F-rich hydrothermal fluids that are intimately associated with highly fractionated granites (e.g., Audétat et al., 2000; Berni et al., 2017) remain poorly

understood. The earliest-crystallized scheelites in various magmatic-hydrothermal deposits frequently exhibit comparable REE patterns to the associated granitoids and record the information of initial ore-forming fluids (e.g., Sun and Chen, 2017; Li et al., 2018; Su et al., 2019; Sun et al., 2019). The earliest-formed Sch_Q 2 that coexists with fluorite in the Weijia W skarn deposit shows flat REE patterns without obvious LREE/HREE fractionation and is strongly depleted in Eu (Fig. 11a). These signatures are identical to those of the host granite porphyry (Fig. 11a). Compared with the stage-3 and stage-4 scheelites (Fig. 11b–e), the Sch_Q 2 might have reflected the features of primary F-rich mineralizing fluids.

Experimental data for the partition coefficients of REEs between scheelite and hydrothermal fluids (DSch/fluid REEs) are not available. Brugger et al. (2000) estimated apparent DSch/fluid REEs values for the scheelite involving Na-coupled REE substitution in orogenic gold deposits. The ideal REE^{3+} radius for the Nb-coupled substitution (1.06 Å, Sun et al., 2019) is the same as that for the Na-coupled substitution (1.06 Å, Ghaderi et al., 1999). Thus, it can be speculated that these two mechanisms of REE substitution will bring about comparable variation trends of DSch/fluid REEs from La to Lu. Using the minimum (model 1) and maximum (model 2) DSch/fluid REEs values of Brugger et al. (2000), the REE compositions of primary F-rich magmatic fluids in equilibrium with the Sch_Q 2 are calculated with presumed fluid Eu^{2+}/Eu^{3+} ratios of 0.4, 4, and 40 (Table S7). As shown in Fig. 11f, the primary F-rich magmatic fluids are inferred to have similar LREE/HREE fractionation to the granite porphyry but with overall higher ΣREE concentrations.

Alternatively, the REE compositions of primary F-rich magmatic fluids can also be acquired based on the compositions of granitic melts and the DFluid/melt REEs. However, most DFluid/melt REEs data are applicable to Cl-rich hydrothermal fluids (e.g., Flynn and Burnham, 1978; Kravchuk et al., 1995; Reed et al., 2000). Considering that the primary mineralizing fluids

mimic the fluoride hydrosaline melts in F- and W-enriched signatures (Veksler, 2005), the minimum liquid-liquid DFluoride/silicate REEs values of Veksler et al. (2012) are adopted as the DFluid/melt REEs. Because both LREE-enriched minerals (e.g., monazite, parisite, and apatite) and HREE-enriched minerals (e.g., xenotime, samarskite, and fergusonite) were crystallized probably before the exsolution of F-rich fluids, the REE compositions of granitic melts in equilibrium with exsolving F-rich fluids are calculated by subtracting hypothetical proportions of 10%, 50%, and 80% REEs from the granite porphyry (Table S7). As a consequence, the inferred F-rich magmatic-hydrothermal fluids (model 3) show similar REE patterns to the granite porphyry but with higher ΣREE concentrations as well (Fig. 11f).

Theoretical prediction advocates that in aqueous solutions the chloride complexes of LREEs are more stable than those of HREEs whereas the fluoride complexes of HREEs are more stable than those of LREEs (Wood, 1990; Haas et al., 1995). The experimental study of Tsay et al. (2014) also has revealed that the Cl-rich and F-rich aqueous fluids prefer to dissolve LREEs and HREEs, respectively. The Cl-rich fluids have higher DFluid/melt LREEs and lower DFluid/melt HREEs (Flynn and Burnham, 1978; Kravchuk et al., 1995; Reed et al., 2000) and generally exhibit stronger LREE/HREE fractionation than the related granitoids (e.g., Banks et al., 1994). The F-rich fluids tend to have lower LREE/HREE ratios than the Cl-rich fluids and display similar REE patterns to the associated granites. Therefore, it can be concluded that in the Weijia W skarn deposit the earlier exsolved Cl-rich fluids are LREE-enriched and HREE-depleted whereas the later exsolved F-rich fluids have relatively flat REE patterns without obvious LREE/HREE fractionation.

6.3. Diffusive vs. advective metasomatism and skarn formation

The formation of a skarn deposit generally includes the following four stages: (1) wall-rock metamorphism; (2) wall rock-controlled reaction skarn/skarnoid by metamorphic recrystallization

and diffusive metasomatism; (3) magmatic fluid-controlled metasomatic skarn by advective metasomatism; (4) retrograde alteration of the metamorphic and metasomatic calc-silicate assemblages possibly involving exotic fluids (Einaudi et al., 1981; Meinert et al., 2005). The diffusive metasomatism is driven by the chemical potential gradients in pore solutions under low water/rock (W/R) ratios and is inefficient in the transport of components, while the advective metasomatism is characterized by pressure gradient-forced fluid flow along percolation paths under high W/R ratios and can efficiently transport the chemical components (Korzhinskii, 1968; Joesten, 1977; Norton, 1987; Zharikov and Rusinov, 1998). Fracturing of rocks at depth in the crust will generate elevated permeability and facilitate the high fluid flux necessary to produce mineralized skarn system by advective metasomatism (Cox, 2005; Rubenach, 2013). The change in hydrothermal dynamics during fluid-rock interaction will result in significant compositional variation of skarn minerals (e.g., Gaspar et al., 2008; Wen et al., 2020).

The Grt_C 1 from the Weijia W deposit shows mildly LREE-enriched and HREE-depleted REE patterns without obvious Eu anomalies (Fig. 9a). These signatures are identical to those of the host limestone (Fig. 9a). The Grt_C 1 is also akin to the host limestone in ΣREE contents although some grains are slightly richer in REEs (Fig. 9a). It is evident that the stage-1 calcic skarn is dominantly controlled by wall-rock compositions. The distinctly higher W contents of the Grt_C 1 than those of the host limestone (Fig. 10b) and the slightly higher ΣREE contents of some Grt_C 1 grains (Fig. 9a) support an input of magmatic fluids, but the W/R ratio should be low. Combined with the disseminated occurrence of the Grt_C 1 (Fig. 3c and d), it is concluded that the stage-1 calcic skarnization was facilitated by diffusive metasomatism.

Compared with the host dolostone, the Grt_M 1A has distinctly higher LREE contents and clearer Eu depletions but similar HREE (Gd–Er) contents except for the upward convex of Tm-Yb-Lu (Fig. 9c) which is ascribed to the YAG-type REE substitution, indicating involvement

of more Cl-rich magmatic fluids during the formation of the Grt_M 1A relative to the Grt_C 1. The generation of cracks in wall rocks will cause a drop of fluid pressure which in turn lead to the infiltration of magmatic fluids along the cracks down pressure gradient with higher W/R ratios. The Grt_M 1A is distributed within the stockwork veinlets that are favorable for the influx of magmatic fluids. The increasing ΣREE contents and intensifying Eu negative anomalies from the Grt_M 1A to the Grt_M 1B (Fig. 9c) are symptomatic of an elevating W/R ratio. From the host dolostone through the Grt_M 1A to the Grt_M 1B, the greater increase of LREEs relative to that of HREEs (Fig. 9c) signifies that the REEs entering the Grt_M 1 retain the LREE-enriched and HREE-depleted features of the Cl-rich magmatic fluids. This likely reflects a disequilibrium state between the Grt_M 1 and Cl-rich fluids because the grossularitic garnet equilibrated with fluids can be theoretically predicted to display smaller increase in LREEs than that in HREEs owing to the strikingly lower DGrs/fluid LREEs and higher DGrs/fluid HREEs (Smith et al., 2004; Gaspar et al., 2008; Xu et al., 2020). The disequilibrium crystallization was probably induced by rapid growth of garnet which will commonly result in oscillatory zonation, such as those observed in the Grt_C 1 and Grt_M 1A (Fig. 6a and e), on account of the dynamic interaction between the growing garnet and the surface layer (Smith et al., 2004; Gaspar et al., 2008; Park et al., 2017; Xiao et al., 2018; Fei et al., 2019).

In contrast to the host limestone and dolostone, the Grt_C 3 and Grt_M 3 exhibit distinctly higher HREE contents and stronger Eu depletions (Fig. 9b and d) which are apparently affinitive with the F-rich magmatic fluids (Fig. 11f), manifesting a dominant control of magmatic fluids on the formation of the stage-3 skarns. Combined with the stockwork occurrence of the Grt_C 3 (Fig. 3c and d) and the inside-stockwork distribution of the Grt_M 3, it is evident that the stage-3 skarnization was promoted by advective metasomatism in fluid-dominant environments with high W/R ratios. The chaotic boundary between the Grt_M 3A and Grt_M 3B (Fig. 6f) is suggestive of a

476 turbulent hydrothermal dynamic state, supporting fluid advection as well. The Grt_M 3A replaces
477 the Grt_M 1B (Fig. 6d and e) and thus the high contents of LREEs in the Grt_M 3A (Fig. 9d) are in
478 all probability inherited from the Grt_M 1B (Fig. 9c). The REE patterns of the Grt_M 3B and Grt_C 3
479 present striking depletions of LREEs with low $(La/Sm)_N$ ratios and relatively flat HREE shapes
480 (Figs. 9b, d and 10a). They are consistent with the variation trends of DGrt/fluid REEs from La to
481 Lu for Al-rich to intermediate grandite (Smith et al., 2004; Gaspar et al., 2008; Xu et al., 2020),
482 indicating an equilibrium state between the Grt_C 3 and Grt_M 3B and the F-rich magmatic fluids.
483 The absence of oscillatorily zoned texture in the Grt_C 3 and Grt_M 3B (Fig. 6b and f) is possibly
484 reflective of relatively low growth rates that are beneficial to the equilibrium with fluids. The
485 lower $(La/Sm)_N$ ratios and higher HREE contents of the grossularitic Grt_M 3B than those of the
486 less Al-rich Grt_C 3 (Figs. 9b, d and 10a) can be well explained by the steeper increase of
487 DGrt/fluid LREEs from La to Sm and higher DGrt/fluid HREEs for more Al-rich grandite (Smith
488 et al., 2004; Xu et al., 2020).

489 The stage-4 skarnization is mainly presented as stockwork pyroxene in the calcic skarn (Fig.
490 3c and d) and stockwork phlogopite and serpentine in the magnesian skarn (Fig. 3e and f) and is
491 much more extensive than the stage-3 skarnization (Fig. 3d–f). The stage-4 skarns contain much
492 more hydrous minerals (phlogopite, serpentine, and chlorite, etc.) than the stage-3 skarns. These
493 differences evidently manifest that the stage-4 skarns were formed through more intense
494 fluid-rock interaction by advective metasomatism. Remarkably, the magnesian skarn is more
495 enriched in volatiles relative to the calcic skarn. The magnesian skarn garnet is richer in F than
496 the calcic skarn garnet in the same stage (Table S1) and the stage-4 magnesian skarn contains
497 much more hydrous minerals (phlogopite and serpentine, Fig. 5e–h) than the stage-4 calcic skarn
498 (chlorite, Fig. 5d), implying a higher W/R ratio for the magnesian skarnization relative to the

499 calcic skarnization. This is probably related to the greater depth of the magnesian skarn (Fig. 2)
500 and thus the volatile components are more difficult to escape under elevated pressure conditions.

501 **6.4. Fluid evolution and W skarn mineralization**

502 Numerous previous studies have revealed that the changes in fluid compositions and
503 physicochemical conditions (e.g., P, T, f_{O_2}, and pH) by fluid-rock interaction, mineral
504 precipitation, fluid mixing, natural cooling, and structural depressurization essentially control the
505 process of skarn mineralization (e.g., Baker et al., 2004; Ismail et al., 2014; Xiao et al., 2018;
506 Ryan-Davis et al., 2019; Tian et al., 2019; Chen et al., 2020b). Probably multi-stage fluid
507 exsolution is another critical factor affecting the skarn ore-forming process. Experimental
508 investigations show that W partitions in favor of the melts with high F concentrations (Manning
509 and Henderson, 1984; Keppler and Wyllie, 1991) and the addition of Cl will not change the
510 DFluid/melt W (Wood and Vlassopoulos, 1989; Keppler and Wyllie, 1991). Recently, Wang et
511 al. (2021) found that W is dissolved predominantly as $H_3WO_4F–2$ in F-rich aqueous solutions.
512 Hence, the W concentration in the residual melts would not be reduced until the extensive
513 exsolution of F-rich fluids. The earlier exsolved Cl-rich fluids is generally relatively poor in W
514 and are not beneficial to W mineralization (e.g., Audétat et al., 2000). The high contents of W in
515 the Grt_C 1 (up to 1181 ppm, Fig. 10b) are attributed to its andraditic compositions instead of
516 reflecting a high W concentration in the Cl-rich fluids. The W and andradite contents of the
517 Weijia garnets display a clear positive correlation (Fig. 10b). Such positive correlation is also
518 frequently observed in other skarn deposits (e.g., Park et al., 2017; Ding et al., 2018; Fei et al.,
519 2019; Chen et al., 2020b). The grossularitic Grt_M 1 has very low W contents (as low as 0.42 ppm,
520 Fig. 10b). Thus, in the Weijia W skarn deposit, the earlier exsolution of Cl-rich magmatic fluids

had not led to the precipitation of scheelite and the W mineralization dominantly followed the later exsolution of F-rich magmatic fluids.

The existence of fluorine in magmatic-hydrothermal fluids has a significant effect on the fluid nature. Fluorine is a hard base (ligand) in the Pearson classification and prefers to bond electrostatically to form aqueous complexes with hard acids, such as REEs, Y, Nb, and Ta, thereby raising the solubilities of these elements in aqueous solutions (Wood, 1990; Haas et al., 1995; Zaraisky et al., 2010; Linnen et al., 2014; Tsay et al., 2014; Timofeev et al., 2015, 2017). Therefore, REEs, Y, Nb, and Ta will partition considerably into the fluid phase during the exsolution of F-rich hydrothermal fluids. The Sch_Q 2 has remarkably higher ΣREE, Y, Nb, and Ta contents than the stage-3 and stage-4 scheelites (Fig. 12b and c) and also most scheelites from other magmatic-hydrothermal deposits (e.g., Li et al., 2018; Poulin et al., 2018; Zhang et al., 2018; Zhao et al., 2018; Sun et al., 2019), corroborating that the primary F-rich mineralizing fluids are enriched in these trace elements.

The low Ce^{4+}/Ce^{3+} ratios (0.94–10) and δEu values (0.02–0.55) of zircon from the Weijia granite porphyry manifest a low magmatic oxygen fugacity (f_{O_2}) (Zhao et al., 2016). The Mo content of scheelite is an effective redox proxy and the low scheelite Mo contents indicate relatively reducing conditions since oxidized Mo (Mo^{6+}, 0.41 Å) tends to enter the scheelite lattice by substituting for W^{6+} (0.42 Å) whereas reduced Mo (Mo^{4+}, 0.65 Å) does not (Song et al., 2014; Poulin et al., 2018; Han et al., 2020). The Mo contents of the Sch_Q 2 (mostly < 1000 ppm, Fig. 12d) are much lower than those formed under oxidizing conditions (e.g., King Island) and are similar to those formed under reducing conditions (e.g., Shimensi) (Fig. 6 in Sun and Chen, 2017), suggesting a reducing condition. Manganese is a redox-sensitive element and Mn^{2+} (0.96 Å) is readily to substitute for Ca^{2+} (1.12 Å) in scheelite (Poulin et al., 2018). The negative

correlation between the Mn and Mo contents of the Weijia scheelites (Fig. 12d) implies that the Mn content of scheelite is a potential redox proxy, with high scheelite Mn contents pointing to relatively reducing conditions, just as the Mn-in-apatite oxybarometer (Miles et al., 2014). The Sch_Q 2 contains up to 1977 ppm Mn (Fig. 12d) which is distinctly higher than the scheelite Mn contents of various deposit types (< 100 ppm) complied by Poulin et al. (2018), supporting a reducing condition as well. In combination with the coexistence between the Sch_Q 2 and molybdenite (Mo^{4+}) (Fig. 7a), it is concluded that the primary F-rich magmatic fluids are reduced.

The assemblage of andraditic Grt_C 1 (Fe exists as Fe^{3+}, Fig. 8a) and diopsidic Px_C 1 (Fig. 8c) in the limestone implies a relatively oxidizing environment (Meinert et al., 2005). However, the Cl-rich fluids derived from the reduced granitic magmas can be expected to be reduced. The Sch_C 3 and Sch_M 3 within the carbonate strata have higher Mo and lower Mn contents than the Sch_Q 2 within the granite porphyry (Fig. 12d), denoting an elevating fluid f_{O_2} during the interaction between the reduced F-rich magmatic fluids and the carbonate strata. Hence, it is deduced that there was a storage of oxidizing fluids in the carbonate wall rocks. In all probability, the oxidizing fluids at a shallow crustal level were meteoric waters that are commonly involved in the formation of skarn deposits (Einaudi et al., 1981; Meinert et al., 2005, e.g., Zhao et al., 2018; Park et al., 2019; Ryan-Davis et al., 2019). The change of REE substitution mechanism from $Ca^{2+} + Fe^{3+} = REE^{3+} + Mg^{2+}$ for the andraditic Grt_C 1 (Fig. 13a) to $Ca^{2+} + Al^{3+} = REE^{3+} + Fe^{2+}$ for the less Fe-rich Grt_C 3 (Fig. 13b) signifies the transition of a Fe^{3+}-dominant state into a Fe^{2+}-prevalent state of the Fe in fluids and thus a depressing fluid f_{O_2}. The fluid f_{O_2} depends on the relative proportions of the reduced magmatic fluids and the oxidized meteoric waters. The

566 reduction of fluids from the stage-1 to stage-3 skarnization is consistent with the increasing influx
567 of reduced magmatic fluids as discussed above.

568 The Sch_C 3 and Sch_M 3 are comparable to the Sch_Q 2 in REE patterns (Fig. 11a–b and d) and
569 REE substitution mechanisms (Fig. 14), manifesting that the stage-3 fluids are inherited from the
570 stage-2 fluids. Nevertheless, the lower ΣREE, Y, Nb, and Ta contents of the Sch_C 3 and Sch_M 3
571 than those of the Sch_Q 2 (Fig. 12b and c) indicate that the stage-3 fluids are relatively evolved
572 than the stage-2 fluids. On the one hand, the precipitation of fluorite during the stage 2 consumed
573 a fraction of F which would depress the solubilities of REEs, Y, Nb, and Ta in fluids. On the
574 other hand, the Sch_Q 2 had taken away a certain amount of these trace elements. The Sch_C 3 and
575 Sch_M 3 coexist with the stage-3 garnets (Figs. 5c, e and 6b, d–e). The coexisting garnets that
576 contain REEs, Y, Nb, and Ta (Table S3) partly account for the lower contents of these trace
577 elements in the Sch_C 3 and Sch_M 3 relative to those in the Sch_Q 2 (Fig. 12b and c). The Grt_C 3 is
578 depleted in LREEs (Fig. 9b), therefore, the coexisting Sch_C 3 has higher $(La/Yb)_N$ ratios than the
579 Sch_Q 2 (Figs. 11a–b and 12a). The Grt_M 3A and Grt_M 3B display relatively flat and
580 LREE-depleted REE patterns, respectively (Fig. 9d), as a result, some grains of the coexisting
581 Sch_M 3 have similar $(La/Yb)_N$ ratios to the Sch_Q 2 and some grains show higher $(La/Yb)_N$ ratios
582 than the Sch_Q 2 (Figs. 11a, d and 12a).

583 The Sch_C 4 and Sch_M 4 have strikingly lower ΣREE, Y, Nb, and Ta contents than the Sch_Q 2,
584 Sch_C 3, and Sch_M 3 (Fig. 12b and c). Compared with the stage-2 and stage-3 scheelites, the
585 stage-4 scheelites are strongly HREE-depleted without obvious Eu anomalies and apparently
586 deviate from the primary F-rich magmatic fluids in REE patterns (Fig. 11). These differences
587 signify that the stage-4 scheelites were crystallized from evidently evolved mineralizing fluids.
588 The scheelite precipitated from oxidized fluids will produce a diagonal Eu_N vs. Eu* N array with
589 a slope of +1 as Eu^{3+} follows Sm^{3+} and Gd^{3+}, while the scheelite crystallized in reduced fluids

will yield a horizontal array because Eu^{2+} is decoupled from Sm^{3+} and Gd^{3+} (Ghaderi et al., 1999). As clearly shown in Fig. 16, the Sch_C 4 and Sch_M 4 were formed in the fluids with $Eu^{3+} \gg Eu^{2+}$, manifesting that the evolved stage-4 fluids are oxidized. The increasing Mo contents from the Sch_C 3 to Sch_C 4 and the decreasing Mn contents from the Sch_M 3 to Sch_M 4 (Fig. 12d) also support an elevating fluid f_{O_2}. The oxidation of fluids from the stage-3 to stage-4 skarnization reflects an increasing influx of meteoric waters during the process of fluid evolution.

Both the Nb and Ta solubilities in fluids decrease with decreasing F concentration at high-F conditions and are constant at low-F conditions, and the Ta solubility is lower than the Nb solubility at the same F content and shifts into the constant state more readily than the latter with decreasing F concentration (Timofeev et al., 2015, 2017). In the Weijia W deposit, the Nb and Ta contents of the Sch_Q 2, Sch_C 3, and Sch_M 3 are concurrently decreasing, while the Ta contents of the Sch_C 4 and Sch_M 4 are almost constant as the Nb contents decrease (Fig. 12c), implying that the stage-4 fluids are relatively depleted in F than the stage-2 and stage-3 fluids. The phlogopite in the stage-4 magnesian skarn has F contents of 2.65–6.88 wt% (Table S6). Using the phlogopite fluorimeter of Aksyuk (2000), the HF concentrations of the stage-4 fluids are estimated to be $10^{-3.0}$ to $10^{-2.6}$ mol/L and are distinctly lower than those of the primary F-rich magmatic fluids ($10^{-2.3}$ to $10^{-1.0}$ mol/L), revealing a decreased fluid F activity. The consumption of fluorine by the formation of fluorite and the other F-rich minerals largely controls the compositional evolution of the F-rich ore-forming fluids. The decrease of F concentration can depress the solubilities and thus the concentrations of REEs, Y, Nb, and Ta in fluids. Moreover, the reduced F concentration in fluids would lead to stronger depletions of HREEs than those of LREEs since the influence of F on the solubilities of HREEs is stronger than those of LREEs (Wood, 1990; Haas et al., 1995; Tsay et al., 2014).

The Grt_C 3, Grt_M 3, Sch_C 3, and Sch_M 3 contain considerable amounts of REEs, Y, Nb, Ta and are all obviously Eu-depleted (Figs. 9, 11, 12 and Table S3). The crystallization of the stage-3 garnets and scheelites would cause the depletions of REEs, Y, Nb, Ta and a relative enrichment of Eu in the remaining stage-4 fluids. The increasing influx of meteoric waters would dilute the mineralizing fluids and raise the DSch/fluid Eu due to the elevating fluid f_{O_2} (Brugger et al., 2000; Li et al., 2018). The relative enrichment of Eu in the stage-4 fluids and the increased DSch/fluid Eu account for the increased δEu values of the Sch_C 4 and Sch_M 4 (Fig. 12a). The HREE-depleted signature of the Sch_C 4 (Fig. 11c) is partly ascribed to its coexisting Px_C 4 owing to the lower DCpx/fluid LREEs and higher DCpx/fluid HREEs (Zhao et al., 2018; Wen et al., 2020). The existence of the Px_C 4 is also responsible for the higher $(La/Yb)_N$ ratios of the Sch_C 4 than those of the Sch_M 4 (Fig. 12a).

Scheelite precipitation is commonly considered as a result of fluid-rock interaction (e.g., Song et al., 2014; Sun and Chen, 2017; Li et al., 2018; Zhang et al., 2018; Sun et al., 2019; Han et al., 2020). We propound that the neutralization of acidic magmatic fluids and the release of Ca from host rocks during fluid-rock interaction are critical for the precipitation of scheelite in the Weijia W deposit. The W-bearing magmatic-hydrothermal fluids are generally acidic (Wood and Samson, 2000). It is well known that greisen is mostly the alteration product of granitic rocks by acidic F-rich magmatic fluids (Shcherba, 1970; Burt, 1981; Štemprok, 1987; Launay et al., 2021). The Sch_Q 2 within the granite porphyry is closely associated with greisenization, implying that the primary F-rich magmatic fluids in the Weijia W deposit should be acidic. Both the transformation of feldspars to muscovite during greisenization ($3KAlSi_3O_8 + 2H^+ = KAl_3Si_3O_{10}(OH)_2 + 6SiO_2 + 2K^+$; $3NaAlSi_3O_8 + 2H^+ + K^+ = KAl_3Si_3O_{10}(OH)_2 + 6SiO_2 + 3Na^+$; $3CaAl_2Si_2O_8 + 4H^+ + 2K^+ = 2KAl_3Si_3O_{10}(OH)_2 + 3Ca^{2+}$) and the decomposition of calcite and

dolomite during skarnization ($CaCO_3 + 2H^+ = Ca^{2+} + H_2O + CO_2$; $CaMg(CO_3)_2 + 4H^+ = Ca^{2+} + Mg^{2+} + 2H_2O + 2CO_2$) are acid-consuming reactions and raise the pH value of mineralizing fluids. The variation of fluid pH largely controls the dominant tungsten species and also significantly affects the tungsten solubility (Wood and Samson, 2000; Wang et al., 2019, 2021). The solubility of scheelite in fluids with near-neutral pH is lower than those in acidic and alkaline fluids, and thus near-neutral fluid pH condition is more beneficial to scheelite precipitation (Wang et al., 2019). The precipitation of scheelite took place in both reducing (Sch_Q 2) and oxidizing (Sch_C 4 and Sch_M 4) environments, therefore, the change of fluid f_{O_2} is not the trigger for scheelite precipitation.

A sufficient supply of Ca is crucial for scheelite mineralization. The Weijia granite porphyry has very low CaO contents (mostly < 1 wt%, Zhao et al., 2016; Huang et al., 2017; Wu et al., 2021) and the plagioclase therein is albite (An < 5). The amount of Ca released through the weak greisenization of granite porphyry is small. This could be decisive for the economic unimportance of the scheelite-bearing stockwork quartz veinlets in the Weijia W deposit. However, Ca is oversupplied by the carbonate wall rocks during the process of skarnization even though large amounts of calc-silicate minerals and fluorite are formed. Hence, the economically significant W mineralization of the Weijia W deposit dominantly occurs in the calcic and magnesian skarns. Additionally, the decrease of fluid pressure by stockwork fracturing promoted the liberation of Ca from the carbonate wall rocks by CO_2 escape and then facilitated the scheelite mineralization, although the tungsten solubility is only weakly dependent on pressure (Wood and Samson, 2000).

7. Conclusions

In this study, trace element geochemistry of garnet and scheelite is applied to constrain the processes of fluid evolution and W skarn mineralization in the F-rich Weijia W deposit. We advocate that a combined study of multiple minerals will provide us with a more comprehensive view into the ore-forming processes. The main conclusions are summarized as follows:

(1) An earlier exsolution of Cl-rich magmatic fluids and a later exsolution of F-rich magmatic fluids are recognized in the Weijia W skarn deposit. The Cl-rich fluids are LREE-enriched and HREE-depleted and bring about pre-ore skarnization, while the F-rich fluids have relatively flat REE patterns without obvious LREE/HREE fractionation and are responsible for W mineralization;

(2) The process of skarn formation in the Weijia W deposit is characterized by a shift from more diffusive to more advective metasomatism with an elevating water/rock ratio. The advective metasomatism with a high flux of mineralizing fluids is hydrodynamically favorable for the consequent ore deposition;

(3) The consumption of fluorine in the ore-forming fluids decreased the ΣREE, Y, Nb, Ta concentrations and enhanced the LREE/HREE fractionation. The oxygen fugacity of ore-forming fluids was increased with the influx of meteoric waters. Scheelite precipitation was triggered by the neutralization of acidic W-bearing fluids and the liberation of Ca from host rocks through fluid-rock interaction.

Acknowledgements

We are grateful to Jian-Feng Gao for his enlightening discussions during the process of manuscript preparation. Xiao-Yu Li and Qiang Zhang are thanked for their suggestions on the explanation of scheelite trace element data. Two anonymous referees provide helpful comments and suggestions that improve this manuscript. This work was financially supported by the National Natural Science Foundation of China (Grant Nos. 41830428 and 41903039),

682 Fundamental Research Funds for the Central Universities (Grant No. DLTD2104), China
683 Postdoctoral Science Foundation (Grant No. 2019M661792), and Sino-French Cai Yuanpei
684 Program of China Scholarship Council.

685 **References**

686 Aksyuk, A.M., 2000. Estimation of fluorine concentrations in fluids of mineralized skarn
687 systems. Econ. Geol. 95, 1339–1347. https://doi.org/10.2113/gsecongeo.95.6.1339.
688 Audétat, A., Günther, D., Heinrich, C.A., 2000. Magmatic-hydrothermal evolution in a
689 fractionating granite: A microchemical study of the Sn-W-F-mineralized Mole Granite
690 (Australia). Geochim. Cosmochim. Acta 64, 3373–3393.
691 https://doi.org/10.1016/S0016-7037(00)00428-2.
692 Baker, T., van Achterberg, E., Ryan, C.G., Lang, J.R., 2004. Composition and evolution of ore
693 fluids in a magmatic-hydrothermal skarn deposit. Geology 32, 117–120.
694 https://doi.org/10.1130/G19950.1.
695 Banks, D.A., Yardley, B.W.D., Campbell, A.R., Jarvis, K.E., 1994. REE composition of an
696 aqueous magmatic fluid: A fluid inclusion study from the Capitan Pluton, New Mexico,
697 U.S.A. Chem. Geol. 113, 259–272. https://doi.org/10.1016/0009-2541(94)90070-1.
698 Berni, G.V., Wagner, T., Fusswinkel, T., Wenzel, T., 2017. Magmatic-hydrothermal evolution of
699 the Kymi topaz granite stock, SE Finland: Mineral chemistry evidence for episodic fluid
700 exsolution. Lithos 292–293, 401–423. https://doi.org/10.1016/j.lithos.2017.09.015.
701 Boynton, W.V., 1984. Cosmochemistry of the rare earth elements: meteorite studies, in:
702 Henderson, P. (Ed.), Rare Earth Element Geochemistry. Elsevier, Amsterdam, pp. 63–114.
703 https://doi.org/10.1016/B978-0-444-42148-7.50008-3.
704 Brugger, J., Lahaye, Y., Costa, S., Lambert, D., Bateman, R., 2000. Inhomogeneous distribution
705 of REE in scheelite and dynamics of Archaean hydrothermal systems (Mt. Charlotte and
706 Drysdale gold deposits, Western Australia). Contrib. Mineral. Petrol. 139, 251–264.
707 https://doi.org/10.1007/s004100000135.
708 Burt, D.M., 1981. Acidity-salinity diagrams–application to greisen and porphyry deposits. Econ.

709 Geol. 76, 832–843. https://doi.org/10.2113/gsecongeo.76.4.832.
710 Carocci, E., Marignac, C., Cathelineau, M., Truche, L., Poujol, M., Boiron, M.-C., Pinto, F.,
711 2021. Incipient wolframite deposition at Panasqueira (Portugal): W-rutile and tourmaline
712 compositions as proxies for the early fluid composition. Econ. Geol. 116, 123–146.
713 https://doi.org/10.5382/econgeo.4783.
714 Černý, P., Blevin, P.L., Cuney, M., London, D., 2005. Granite-related ore deposits. Economic
715 Geology 100th Anniversary Volume, 337–370. https://doi.org/10.5382/AV100.12.
716 Chen, G.H., Gao, J.F., Lu, J.J., Zhang, R.Q., 2020a. In situ LA-ICP-MS analyses of mica and
717 wolframite from the Maoping tungsten deposit, southern Jiangxi, China. Acta Geochim. 39,
718 811–829. https://doi.org/10.1007/s11631-020-00423-5.
719 Chen, J., Lu, J.J., Chen, W.F., Wang, R.C., Ma, D.S., Zhu, J.C., Zhang, W.L., Ji, J.F., 2008.
720 W-Sn-Nb-Ta-bearing granites in the Nanling Range and their relationship to
721 metallogengesis. Geol. J. China Univ. 14, 459–473 (in Chinese with English abstract).
722 https://doi.org/10.3969/j.issn.1006-7493.2008.04.001.
723 Chen, J., Wang, R.C., Zhu, J.C., Lu, J.J., Ma, D.S., 2013. Multiple-aged granitoids and related
724 tungsten-tin mineralization in the Nanling Range, South China. Sci. China Earth Sci. 56,
725 2045–2055. https://doi.org/10.1007/s11430-013-4736-9.
726 Chen, L., Qin, K.Z., Li, G.M., Li, J.X., Xiao, B., Zhao, J.X., 2020b. In situ major and trace
727 elements of garnet and scheelite in the Nuri Cu-W-Mo deposit, South Gangdese, Tibet:
728 Implications for mineral genesis and ore-forming fluid records. Ore Geol. Rev. 122, 103549.
729 https://doi.org/10.1016/j.oregeorev.2020.103549.
730 Cox, S.F., 2005. Coupling between deformation, fluid pressures, and fluid flow in ore-producing
731 hydrothermal systems at depth in the crust. Economic Geology 100th Anniversary Volume,
732 39–75. https://doi.org/10.5382/AV100.04.

733 Ding, T., Ma, D.S., Lu, J.J., Zhang, R.Q., 2018. Garnet and scheelite as indicators of multi-stage
734 tungsten mineralization in the Huangshaping deposit, southern Hunan province, China. Ore
735 Geol. Rev. 94, 193–211. https://doi.org/10.1016/j.oregeorev.2018.01.029.
736 Dingwell, D.B., Scarfe, C.M., Cronin, D.J., 1985. The effect of fluorine on viscosities in the
737 system Na_2O-Al_2O_3-SiO_2: implications for phonolites, trachytes and rhyolites. Am. Mineral.
738 70, 80–87.
739 Einaudi, M.T., Meinert, L.D., Newberry, R.J., 1981. Skarn deposits. Economic Geology 75th
740 Anniversary Volume, 317–391. https://doi.org/10.5382/AV75.11.
741 Fei, X.H., Zhang, Z.C., Cheng, Z.G., Santosh, M., 2019. Factors controlling the crystal
742 morphology and chemistry of garnet in skarn deposits: A case study from the Cuihongshan
743 polymetallic deposit, Lesser Xing'an Range, NE China. Am. Mineral. 104, 1455–1468.
744 https://doi.org/10.2138/am-2019-6968.
745 Flynn, R.T., Burnham, C.W., 1978. An experimental determination of rare earth partition
746 coefficients between a chloride containing vapour phase and silicate melts. Geochim.
747 Cosmochim. Acta 42, 685–701. https://doi.org/10.1016/0016-7037(78)90087-X.
748 Gaspar, M., Knaack, C., Meinert, L.D., Moretti, R., 2008. REE in skarn systems: A LA-ICP-MS
749 study of garnets from the Crown Jewel gold deposit. Geochim. Cosmochim. Acta 72, 185–
750 205. https://doi.org/10.1016/j.gca.2007.09.033.
751 Ghaderi, M., Palin, J.M., Campbell, I.H., Sylvester, P.J., 1999. Rare earth element systematics in
752 scheelite from hydrothermal gold deposits in the Kalgoorlie-Norseman region, Western
753 Australia. Econ. Geol. 94, 423–437. https://doi.org/10.2113/gsecongeo.94.3.423.
754 Ghazi, A.M., Vanko, D.A., Roedder, E., Seeley, R.C., 1993. Determination of rare earth elements
755 in fluid inclusions by inductively coupled plasma-mass spectrometry (ICP-MS). Geochim.
756 Cosmochim. Acta 57, 4513–4516. https://doi.org/10.1016/0016-7037(93)90500-V.

757 Grew, E.S., Locock, A.J., Mills, S.J., Galuskina, I.O., Galuskin, E.V., Hålenius, U., 2013.
758 Nomenclature of the garnet supergroup. Am. Mineral. 98, 785–811.
759 https://doi.org/10.2138/am.2013.4201.
760 Grew, E.S., Marsh, J.H., Yates, M.G., Lazic, B., Armbruster, T., Locock, A., Bell, S.W., Dyar,
761 M.D., Bernhardt, H.-J., Medenbach, O., 2010. Menzerite-(Y), a new species,
762 $\{(Y,REE)(Ca,Fe^{2+})_2\}[(Mg,Fe^{2+})(Fe^{3+},Al)](Si_3)O_{12}$, from a felsic granulite, Parry Sound,
763 Ontario, and a new garnet end-member, $\{Y_2Ca\}[Mg_2](Si_3)O_{12}$. Can. Mineral. 48, 1171–
764 1193. https://doi.org/10.3749/canmin.48.5.1171.
765 Haas, J.R., Shock, E.L., Sassani, D.C., 1995. Rare earth elements in hydrothermal systems:
766 Estimates of standard partial molal thermodynamic properties of aqueous complexes of the
767 rare earth elements at high pressures and temperatures. Geochim. Cosmochim. Acta 59,
768 4329–4350. https://doi.org/10.1016/0016-7037(95)00314-P.
769 Han, J.S., Chen, H.Y., Hong, W., Hollings, P., Chu, G.B., Zhang, L., Sun, S.Q., 2020. Texture
770 and geochemistry of multi-stage hydrothermal scheelite in the Tongshankou porphyry-skarn
771 Cu-Mo(-W) deposit, eastern China: Implications for ore-forming process and fluid
772 metasomatism. Am. Mineral. 105, 945–954. https://doi.org/10.2138/am-2020-7194.
773 Hedenquist, J.W., Lowenstern, J.B., 1994. The role of magmas in the formation of hydrothermal
774 ore deposits. Nature 370, 519–527. https://doi.org/10.1038/370519a0.
775 Heinrich, C.A., Candela, P.A., 2014. Fluids and ore formation in the Earth's crust, in: Holland,
776 H.D., Turekian, K.K. (Eds.), Treatise on Geochemistry, second ed. Elsevier, Amsterdam,
777 vol. 13, pp. 1–28. https://doi.org/10.1016/B978-0-08-095975-7.01101-3.
778 Huang, X.D., 2018. Middle-Late Jurassic Cu-Pb-Zn-bearing and W-bearing granitoids and their
779 skarn mineralization in the Nanling Range, South China: the Tongshanling and Weijia
780 deposits (Ph.D. thesis). Nanjing University, Nanjing, pp. 1–330.

https://doi.org/10.27235/d.cnki.gnjiu.2018.000946.

Huang, X.D., Lu, J.J., Sizaret, S., Wang, R.C., Ma, D.S., Zhang, R.Q., Zhao, X., Wu, J.W., 2017. Petrogenetic differences between the Middle-Late Jurassic Cu-Pb-Zn-bearing and W-bearing granites in the Nanling Range, South China: A case study of the Tongshanling and Weijia deposits in southern Hunan Province. Sci. China Earth Sci. 60, 1220–1236. https://doi.org/10.1007/s11430-016-9044-5.

Ismail, R., Ciobanu, C.L., Cook, N.J., Teale, G.S., Giles, D., Schmidt Mumm, A., Wade, B., 2014. Rare earths and other trace elements in minerals from skarn assemblages, Hillside iron oxide-copper-gold deposit, Yorke Peninsula, South Australia. Lithos 184–187, 456–477. https://doi.org/10.1016/j.lithos.2013.07.023.

Jaffe, H.W., 1951. The role of yttrium and other minor elements in the garnet group. Am. Mineral. 36, 133–155.

Joesten, R., 1977. Evolution of mineral assemblage zoning in diffusion metasomatism. Geochim. Cosmochim. Acta 41, 649–670. https://doi.org/10.1016/0016-7037(77)90303-9.

Keppler, H., Wyllie, P.J., 1991. Partitioning of Cu, Sn, Mo, W, U, and Th between melt and aqueous fluid in the systems haplogranite-H_2O–HCl and haplogranite-H_2O–HF. Contrib. Mineral. Petrol. 109, 139–150. https://doi.org/10.1007/BF00306474.

Korzhinskii, D.S., 1968. The theory of metasomatic zoning. Miner. Depos. 3, 222–231. https://doi.org/10.1007/BF00207435.

Kravchuk, I.F., Ivanova, G.F., Varezhkina, N.S., Malinin, S.D., 1995. REE fractionation in acid fluid-magma systems. Geochem. Int. 32, 60–68.

Launay, G., Sizaret, S., Lach, P., Melleton, J., Gloaguen, É., Poujol, M., 2021. Genetic relationship between greisenization and Sn-W mineralizations in vein and greisen deposits: Insights from the Panasqueira deposit (Portugal). BSGF-Earth Sci. Bull. 192, 2.

https://doi.org/10.1051/bsgf/2020046.

Legros, H., Marignac, C., Tabary, T., Mercadier, J., Richard, A., Cuney, M., Wang, R.C., Charles, N., Lespinasse, M.-Y., 2018. The ore-forming magmatic-hydrothermal system of the Piaotang W-Sn deposit (Jiangxi, China) as seen from Li-mica geochemistry. Am. Mineral. 103, 39–54. https://doi.org/10.2138/am-2018-6196.

Li, J.D., Li, X.F., Xiao, R., 2019. Multiple-stage tungsten mineralization in the Silurian Jiepai W skarn deposit, South China: Insights from cathodoluminescence images, trace elements, and fluid inclusions of scheelite. J. Asian Earth Sci. 181, 103898. https://doi.org/10.1016/j.jseaes.2019.103898.

Li, X.Y., Gao, J.F., Zhang, R.Q., Lu, J.J., Chen, W.H., Wu, J.W., 2018. Origin of the Muguayuan veinlet-disseminated tungsten deposit, South China: Constraints from in-situ trace element analyses of scheelite. Ore Geol. Rev. 99, 180–194. https://doi.org/10.1016/j.oregeorev.2018.06.005.

Li, Z.X., Li, X.H., 2007. Formation of the 1300-km-wide intracontinental orogen and postorogenic magmatic province in Mesozoic South China: A flat-slab subduction model. Geology 35, 179–182. https://doi.org/10.1130/G23193A.1.

Linnen, R.L., Samson, I.M., Williams-Jones, A.E., Chakhmouradian, A.R., 2014. Geochemistry of the rare-earth element, Nb, Ta, Hf, and Zr deposits, in: Holland, H.D., Turekian, K.K. (Eds.), Treatise on Geochemistry, second ed. Elsevier, Amsterdam, vol. 13, pp. 543–568. https://doi.org/10.1016/B978-0-08-095975-7.01124-4.

Liu, Y.S., Hu, Z.C., Gao, S., Günther, D., Xu, J., Gao, C.G., Chen, H.H., 2008. In situ analysis of major and trace elements of anhydrous minerals by LA-ICP-MS without applying an internal standard. Chem. Geol. 257, 34–43. https://doi.org/10.1016/j.chemgeo.2008.08.004.

London, D., Hervig, R.L., Morgan, G.B. VI, 1988. Melt-vapor solubilities and elemental

partitioning in peraluminous granite-pegmatite systems: experimental results with Macusani glass at 200 MPa. Contrib. Mineral. Petrol. 99, 360–373. https://doi.org/10.1007/BF00375368.

Manning, D.A.C., 1981. The effect of fluorine on liquidus phase relationships in the system Qz-Ab-Or with excess water at 1kb. Contrib. Mineral. Petrol. 76, 206–215. https://doi.org/10.1007/BF00371960.

Manning, D.A.C., Henderson, P., 1984. The behaviour of tungsten in granitic melt-vapour systems. Contrib. Mineral. Petrol. 86, 286–293. https://doi.org/10.1007/BF00373674.

Mao, J.W., Cheng, Y.B., Chen, M.H., Pirajno, F., 2013. Major types and time-space distribution of Mesozoic ore deposits in South China and their geodynamic settings. Miner. Depos. 48, 267–294. https://doi.org/10.1007/s00126-012-0446-z.

Mao, J.W., Ouyang, H.G., Song, S.W., Santosh, M., Yuan, S.D., Zhou, Z.H., Zheng, W., Liu, H., Liu, P., Cheng, Y.B., Chen, M.H., 2019. Geology and metallogeny of tungsten and tin deposits in China. Society of Economic Geologists Special Publication 22, 411–482. https://doi.org/10.5382/SP.22.10.

Mao, J.W., Xie, G.Q., Guo, C.L., Chen, Y.C., 2007. Large-scale tungsten-tin mineralization in the Nanling region, South China: Metallogenic ages and corresponding geodynamic processes. Acta Petrol. Sin. 23, 2329–2338 (in Chinese with English abstract). https://doi.org/10.3969/j.issn.1000-0569.2007.10.002.

Meinert, L.D., Dipple, G.M., Nicolescu, S., 2005. World skarn deposits. Economic Geology 100th Anniversary Volume, 299–336. https://doi.org/10.5382/AV100.11.

Miles, A.J., Graham, C.M., Hawkesworth, C.J., Gillespie, M.R., Hinton, R.W., Bromiley, G.D., EMMAC, 2014. Apatite: A new redox proxy for silicic magmas? Geochim. Cosmochim. Acta 132, 101–119. https://doi.org/10.1016/j.gca.2014.01.040.

853 Norman, D.I., Kyle, P.R., Baron, C., 1989. Analysis of trace elements including rare earth
854 elements in fluid inclusion liquids. Econ. Geol. 84, 162–166.
855 https://doi.org/10.2113/gsecongeo.84.1.162.
856 Norton, D.L., 1987. Advective metasomatism, in: Helgeson, H.C. (Ed.), Chemical Transport in
857 Metasomatic Processes. D. Reidel Publishing Company, Dordrecht, pp. 123–132.
858 https://doi.org/10.1007/978-94-009-4013-0_5.
859 Park, C., Choi, W., Kim, H., Park, M.-H., Kang, I.-M., Lee, H.-S., Song, Y., 2017. Oscillatory
860 zoning in skarn garnet: Implications for tungsten ore exploration. Ore Geol. Rev. 89, 1006–
861 1018. https://doi.org/10.1016/j.oregeorev.2017.08.003.
862 Park, C., Park, C., Song, Y., Choi, S.-G., 2019. Sequential trace element analysis of zoned skarn
863 garnet: Implications for multi-stage fluxing and flow of magmatic fluid into a skarn system.
864 Lithos 350–351, 105213. https://doi.org/10.1016/j.lithos.2019.105213.
865 Poulin, R.S., Kontak, D.J., McDonald, A., McClenaghan, M.B., 2018. Assessing scheelite as an
866 ore-deposit discriminator using its trace-element and REE chemistry. Can. Mineral. 56,
867 265–302. https://doi.org/10.3749/canmin.1800005.
868 Reed, M.J., Candela, P.A., Piccoli, P.M., 2000. The distribution of rare earth elements between
869 monzogranitic melt and the aqueous volatile phase in experimental investigations at 800 °C
870 and 200 MPa. Contrib. Mineral. Petrol. 140, 251–262.
871 https://doi.org/10.1007/s004100000182.
872 Røhr, T.S., Austrheim, H., Erambert, M., 2007. Stress-induced redistribution of yttrium and
873 heavy rare-earth elements (HREE) in garnet during high-grade polymetamorphism. Am.
874 Mineral. 92, 1276–1287. https://doi.org/10.2138/am.2007.2479.
875 Rubenach, M., 2013. Structural controls of metasomatism on a regional scale, in: Harlov, D.E.,
876 Austrheim, H. (Eds.), Metasomatism and the Chemical Transformation of Rock. Springer,

Berlin, pp. 93–140. https://doi.org/10.1007/978-3-642-28394-9_4.

Ryan-Davis, J., Lackey, J.S., Gevedon, M., Barnes, J.D., Lee, C.-T.A., Kitajima, K., Valley, J.W., 2019. Andradite skarn garnet records of exceptionally low $\delta^{18}O$ values within an Early Cretaceous hydrothermal system, Sierra Nevada, CA. Contrib. Mineral. Petrol. 174, 68. https://doi.org/10.1007/s00410-019-1602-6.

Shannon, R.D., 1976. Revised effective ionic radii and systematic studies of interatomic distances in halides and chalcogenides. Acta Crystallogr. A32, 751–767. https://doi.org/10.1107/S0567739476001551.

Shcherba, G.N., 1970. Greisens. Int. Geol. Rev. 12, 114–150 & 239–255. https://doi.org/10.1080/00206817009475216.

Shu, L.S., Wang, B., Cawood, P.A., Santosh, M., Xu, Z.Q., 2015. Early Paleozoic and Early Mesozoic intraplate tectonic and magmatic events in the Cathaysia Block, South China. Tectonics 34, 1600–1621. https://doi.org/10.1002/2015TC003835.

Smith, M.P., Henderson, P., Jeffries, T.E.R., Long, J., Williams, C.T., 2004. The rare earth elements and uranium in garnets from the Beinn an Dubhaich aureole, Skye, Scotland, UK: Constraints on processes in a dynamic hydrothermal system. J. Petrol. 45, 457–484. https://doi.org/10.1093/petrology/egg087.

Song, G.X., Qin, K.Z., Li, G.M., Evans, N.J., Chen, L., 2014. Scheelite elemental and isotopic signatures: Implications for the genesis of skarn-type W-Mo deposits in the Chizhou Area, Anhui Province, Eastern China. Am. Mineral. 99, 303–317. https://doi.org/10.2138/am.2014.4431.

Štemprok, M., 1987. Greisenization (a review). Geol. Rundsch. 76, 169–175. https://doi.org/10.1007/BF01820580.

Su, S.Q., Qin, K.Z., Li, G.M., Olin, P., Thompson, J., 2019. Cathodoluminescence and trace

elements of scheelite: Constraints on ore-forming processes of the Dabaoshan porphyry Mo-W deposit, South China. Ore Geol. Rev. 115, 103183. https://doi.org/10.1016/j.oregeorev.2019.103183.

Sun, K.K., Chen, B., 2017. Trace elements and Sr-Nd isotopes of scheelite: Implications for the W-Cu-Mo polymetallic mineralization of the Shimensi deposit, South China. Am. Mineral. 102, 1114–1128. https://doi.org/10.2138/am-2017-5654.

Sun, K.K., Chen, B., Deng, J., 2019. Ore genesis of the Zhuxi supergiant W-Cu skarn polymetallic deposit, South China: Evidence from scheelite geochemistry. Ore Geol. Rev. 107, 14–29. https://doi.org/10.1016/j.oregeorev.2019.02.017.

Tian, Z.D., Leng, C.B., Zhang, X.C., Zafar, T., Zhang, L.J., Hong, W., Lai, C.-K., 2019. Chemical composition, genesis and exploration implication of garnet from the Hongshan Cu-Mo skarn deposit, SW China. Ore Geol. Rev. 112, 103016. https://doi.org/10.1016/j.oregeorev.2019.103016.

Timofeev, A., Migdisov, A.A., Williams-Jones, A.E., 2015. An experimental study of the solubility and speciation of niobium in fluoride-bearing aqueous solutions at elevated temperature. Geochim. Cosmochim. Acta 158, 103–111. https://doi.org/10.1016/j.gca.2015.02.015.

Timofeev, A., Migdisov, A.A., Williams-Jones, A.E., 2017. An experimental study of the solubility and speciation of tantalum in fluoride-bearing aqueous solutions at elevated temperature. Geochim. Cosmochim. Acta 197, 294–304. https://doi.org/10.1016/j.gca.2016.10.027.

Tsay, A., Zajacz, Z., Sanchez-Valle, C., 2014. Efficient mobilization and fractionation of rare-earth elements by aqueous fluids upon slab dehydration. Earth Planet. Sci. Lett. 398, 101–112. https://doi.org/10.1016/j.epsl.2014.04.042.

925 Veksler, I.V., 2005. Element enrichment and fractionation by magmatic aqueous fluids:
926 Experimental constraints on fluid-melt immiscibility and element partitioning, in: Linnen,
927 R.L., Samson, I.M. (Eds.), Rare-Element Geochemistry and Mineral Deposits. Geological
928 Association of Canada, Short Course Notes, vol. 17, pp. 69–85.
929 Veksler, I.V., Dorfman, A.M., Dulski, P., Kamenetsky, V.S., Danyushevsky, L.V., Jeffries, T.,
930 Dingwell, D.B., 2012. Partitioning of elements between silicate melt and immiscible
931 fluoride, chloride, carbonate, phosphate and sulfate melts, with implications to the origin of
932 natrocarbonatite. Geochim. Cosmochim. Acta 79, 20–40.
933 https://doi.org/10.1016/j.gca.2011.11.035.
934 Wang, X.L., Zhou, J.C., Griffin, W.L., Wang, R.C., Qiu, J.S., O'Reilly, S.Y., Xu, X.S., Liu,
935 X.M., Zhang, G.L., 2007. Detrital zircon geochronology of Precambrian basement
936 sequences in the Jiangnan orogen: Dating the assembly of the Yangtze and Cathaysia
937 Blocks. Precambrian Res. 159, 117–131. https://doi.org/10.1016/j.precamres.2007.06.005.
938 Wang, X.S., Timofeev, A., Williams-Jones, A.E., Shang, L.B., Bi, X.W., 2019. An experimental
939 study of the solubility and speciation of tungsten in NaCl-bearing aqueous solutions at 250,
940 300, and 350 °C. Geochim. Cosmochim. Acta 265, 313–329.
941 https://doi.org/10.1016/j.gca.2019.09.013.
942 Wang, X.S., Williams-Jones, A.E., Hu, R.Z., Shang, L.B., Bi, X.W., 2021. The role of fluorine in
943 granite-related hydrothermal tungsten ore genesis: Results of experiments and modeling.
944 Geochim. Cosmochim. Acta 292, 170–187. https://doi.org/10.1016/j.gca.2020.09.032.
945 Webster, J.D., 1992. Water solubility and chlorine partitioning in Cl-rich granitic systems:
946 Effects of melt composition at 2 kbar and 800 °C. Geochim. Cosmochim. Acta 56, 679–687.
947 https://doi.org/10.1016/0016-7037(92)90089-2.
948 Webster, J.D., Holloway, J.R., 1988. Experimental constraints on the partitioning of Cl between

topaz rhyolite melt and H_2O and $H_2O + CO_2$ fluids: New implications for granitic differentiation and ore deposition. Geochim. Cosmochim. Acta 52, 2091–2105. https://doi.org/10.1016/0016-7037(88)90189-5.

Webster, J.D., Holloway, J.R., 1990. Partitioning of F and Cl between magmatic hydrothermal fluids and highly evolved granitic magmas, in: Stein, H.J., Hannah, J.L. (Eds.), Ore-bearing Granite Systems; Petrogenesis and Mineralizing Processes. Geological Society of America, Special Paper, vol. 246, pp. 21–34. https://doi.org/10.1130/SPE246-p21.

Wen, G., Li, J.W., Hofstra, A.H., Koenig, A.E., Cui, B.Z., 2020. Textures and compositions of clinopyroxene in an Fe skarn with implications for ore-fluid evolution and mineral-fluid REE partitioning. Geochim. Cosmochim. Acta 290, 104–123. https://doi.org/10.1016/j.gca.2020.08.020.

Wood, S.A., 1990. The aqueous geochemistry of the rare-earth elements and yttrium: 1. Review of available low-temperature data for inorganic complexes and the inorganic REE speciation of natural waters. Chem. Geol. 82, 159–186. https://doi.org/10.1016/0009-2541(90)90080-Q.

Wood, S.A., Samson, I.M., 2000. The hydrothermal geochemistry of tungsten in granitoid environments: I. Relative solubilities of ferberite and scheelite as a function of T, P, pH, and m_{NaCl}. Econ. Geol. 95, 143–182. https://doi.org/10.2113/gsecongeo.95.1.143.

Wood, S.A., Vlassopoulos, D., 1989. Experimental determination of the hydrothermal solubility and speciation of tungsten at 500 °C and 1 kbar. Geochim. Cosmochim. Acta 53, 303–312. https://doi.org/10.1016/0016-7037(89)90382-7.

Wu, J.H., Kong, H., Li, H., Algeo, T.J., Yonezu, K., Liu, B., Wu, Q.H., Zhu, D.P., Jiang, H., 2021. Multiple metal sources of coupled Cu-Sn deposits: Insights from the Tongshanling polymetallic deposit in the Nanling Range, South China. Ore Geol. Rev. 139, 104521.

https://doi.org/10.1016/j.oregeorev.2021.104521.

Xiao, X., Zhou, T.F., White, N.C., Zhang, L.J., Fan, Y., Wang, F.Y., Chen, X.F., 2018. The formation and trace elements of garnet in the skarn zone from the Xinqiao Cu-S-Fe-Au deposit, Tongling ore district, Anhui Province, Eastern China. Lithos 302–303, 467–479. https://doi.org/10.1016/j.lithos.2018.01.023.

Xu, J., Ciobanu, C.L., Cook, N.J., Zheng, Y.Y., Li, X.F., Wade, B.P., Verdugo-Ihl, M.R., Gao, W.Y., Zhu, Q.Q., 2020. Numerical modelling of rare earth element fractionation trends in garnet: a tool to monitor skarn evolution. Contrib. Mineral. Petrol. 175, 30. https://doi.org/10.1007/s00410-020-1670-7.

Yang, J.H., Peng, J.T., Hu, R.Z., Bi, X.W., Zhao, J.H., Fu, Y.Z., Shen, N.P., 2013. Garnet geochemistry of tungsten-mineralized Xihuashan granites in South China. Lithos 177, 79–90. https://doi.org/10.1016/j.lithos.2013.06.008.

Zaraisky, G.P., Korzhinskaya, V., Kotova, N., 2010. Experimental studies of Ta_2O_5 and columbite-tantalite solubility in fluoride solutions from 300 to 550 °C and 50 to 100 MPa. Miner. Petrol. 99, 287–300. https://doi.org/10.1007/s00710-010-0112-z.

Zhang, Q., Zhang, R.Q., Gao, J.F., Lu, J.J., Wu, J.W., 2018. In-situ LA-ICP-MS trace element analyses of scheelite and wolframite: Constraints on the genesis of veinlet-disseminated and vein-type tungsten deposits, South China. Ore Geol. Rev. 99, 166–179. https://doi.org/10.1016/j.oregeorev.2018.06.004.

Zhang, S.T., Zhang, R.Q., Lu, J.J., Ma, D.S., Ding, T., Gao, S.Y., Zhang, Q., 2019. Neoproterozoic tin mineralization in South China: geology and cassiterite U-Pb age of the Baotan tin deposit in northern Guangxi. Miner. Depos. 54, 1125–1142. https://doi.org/10.1007/s00126-019-00862-y.

Zhang, Y., Yang, J.H., Chen, J.Y., Wang, H., Xiang, Y.X., 2017. Petrogenesis of Jurassic

997 tungsten-bearing granites in the Nanling Range, South China: Evidence from whole-rock
998 geochemistry and zircon U-Pb and Hf-O isotopes. Lithos 278–281, 166–180.
999 https://doi.org/10.1016/j.lithos.2017.01.018.
1000 Zhao, P.L., Yuan, S.D., Mao, J.W., Santosh, M., Li, C., Hou, K.J., 2016. Geochronological and
1001 petrogeochemical constraints on the skarn deposits in Tongshanling ore district, southern
1002 Hunan Province: Implications for Jurassic Cu and W metallogenic events in South China.
1003 Ore Geol. Rev. 78, 120–137. https://doi.org/10.1016/j.oregeorev.2016.03.004.
1004 Zhao, W.W., Zhou, M.F., Li, Y.H.M., Zhao, Z., Gao, J.F., 2017. Genetic types, mineralization
1005 styles, and geodynamic settings of Mesozoic tungsten deposits in South China. J. Asian
1006 Earth Sci. 137, 109–140. https://doi.org/10.1016/j.jseaes.2016.12.047.
1007 Zhao, W.W., Zhou, M.F., Williams-Jones, A.E., Zhao, Z., 2018. Constraints on the uptake of
1008 REE by scheelite in the Baoshan tungsten skarn deposit, South China. Chem. Geol. 477,
1009 123–136. https://doi.org/10.1016/j.chemgeo.2017.12.020.
1010 Zharikov, V.A., Rusinov, V.L., 1998. Metasomatism and Metasomatic Rocks. Nauchnyi Mir,
1011 Moscow (in Russian).
1012 Zhou, X.M., Li, W.X., 2000. Origin of Late Mesozoic igneous rocks in Southeastern China:
1013 implications for lithosphere subduction and underplating of mafic magmas. Tectonophysics
1014 326, 269–287. https://doi.org/10.1016/S0040-1951(00)00120-7.
1015 Zhou, X.M., Sun, T., Shen, W.Z., Shu, L.S., Niu, Y.L., 2006. Petrogenesis of Mesozoic
1016 granitoids and volcanic rocks in South China: A response to tectonic evolution. Episodes 29,
1017 26–33. https://doi.org/10.18814/epiiugs/2006/v29i1/004.

Figure captions

Fig. 1. (a) Map of South China showing the location of the Weijia W skarn deposit. (b) Geological map of the Weijia W skarn deposit.

Fig. 2. West–east-trending geological cross section (section line shown in Fig. 1b) of the Weijia W skarn deposit.

Fig. 3. Representative samples of the (a) granite porphyry and its (b) stockwork quartz veinlets, (c–d) calcic skarn, and (e–f) magnesian skarn from the Weijia W deposit. Mineral abbreviations: Cal = calcite, Grt = garnet, Kfs = K-feldspar, Phl = phlogopite, Px = pyroxene, Qz = quartz, Srp = serpentine, Wo = wollastonite. Subscripts C and M represent calcic and magnesian skarns, respectively, Arabic numerals denote paragenetic stages.

Fig. 4. Petrographic photomicrographs of the granite porphyry and its stockwork quartz veinlets from the Weijia W skarn deposit. (a) Subvolcanic porphyritic texture of the granite porphyry with phenocrysts of quartz, K-feldspar, albite, and biotite (crossed-polarized light, XPL). (b) Interstitial muscovite and muscovite-fluorite aggregates in the matrix of granite porphyry (XPL). (c) Stage-2 scheelite coexisting with fluorite in the stockwork quartz veinlets hosted by weakly greisenized granite porphyry (plane-polarized light, PPL). (d) Altered biotite in the granite porphyry (XPL). Mineral abbreviations: Ab = albite, Bt = biotite, Fl = fluorite, Kfs = K-feldspar, Ms = muscovite, Qz = quartz, Sch = scheelite. Subscript Q represents stockwork quartz veinlets, Arabic numeral denotes paragenetic stage.

Fig. 5. Petrographic photomicrographs of the calcic and magnesian skarns with different generations of garnets and scheelites from the Weijia W deposit. (a) Stage-1 disseminated garnet and pyroxene in the calcic skarn (PPL). (b) The stage-1 garnet enclosing the stage-1 pyroxene and replaced by fluorite in the calcic skarn (BSE). (c) Stage-3 stockwork garnet and associated scheelite in the calcic skarn (PPL). (d) Stage-4 stockwork pyroxene and associated scheelite in

the calcic skarn (XPL). (e) Stage-3 garnet and associated scheelite in the stockwork magnesian skarn (XPL). (f) Stage-4 scheelite coexisting with phlogopite in the stockwork magnesian skarn (XPL). (g) Stage-4 scheelite coexisting with serpentine in the stockwork magnesian skarn (XPL). (h) Stage-1 marialite ($Na_4Al_3Si_9O_{24}Cl$) in the stockwork magnesian skarn (BSE). Mineral abbreviations: Cal = calcite, Chl = chlorite, Dol = dolomite, Fl = fluorite, Grt = garnet, Mar = marialite, Phl = phlogopite, Px = pyroxene, Sch = scheelite, Sel = sellaite, Srp = serpentine, Wo = wollastonite.

Fig. 6. BSE images showing the textures of garnets in the calcic skarn (a–b) and magnesian skarn (c–f). Mineral abbreviations: Fl = fluorite, Grt = garnet, Px = pyroxene, Sch = scheelite. A and B denote two subgenerations of the Grt_M 1 and Grt_M 3.

Fig. 7. (a–d) CL and (e–g) BSE images showing the textures of scheelites in the stockwork quartz veinlets (a), calcic skarn (b–d), and magnesian skarn (e–g). Mineral abbreviations: Fl = fluorite, Mol = molybdenite, Sch = scheelite. Subscripts Q, C, and M represent stockwork quartz veinlets, calcic skarn, and magnesian skarn, respectively, Arabic numerals denote paragenetic stages.

Fig. 8. Major element compositions of different generations of garnets and pyroxenes from the Weijia W skarn deposit. End-member abbreviations: Adr = andradite, Alm = almandine, Di = diopside, Grs = grossular, Hd = hedenbergite, Jhn = johannsenite, Prp = pyrope, Sps = spessartine.

Fig. 9. Chondrite-normalized (Boynton, 1984) REE patterns of different generations of garnets from the Weijia W skarn deposit. The REE data of granite porphyry and carbonate strata are from Huang et al. (2017) and listed in Supplementary Table S5, respectively.

Fig. 10. (a) $(La/Sm)_N$-δEu [$Eu_N/(Sm_N \times Gd_N)^{1/2}$] and (b) Adr (mol%)-W (ppm) binary diagrams of the Weijia garnets. The W data of carbonate strata are listed in Supplementary Table S5.

Fig. 11. Chondrite-normalized (Boynton, 1984) REE patterns of (a–e) different generations of

scheelites and (f) model primary F-rich magmatic fluids in the Weijia W skarn deposit. The REE data of granite porphyry and carbonate strata are from Huang et al. (2017) and listed in Supplementary Table S5, respectively. The model 1 and model 2 of primary F-rich magmatic fluids are calculated based on the mean REE compositions of Sch_Q 2 and the minimum (model 1) and maximum (model 2) DSch/fluid REEs values from Brugger et al. (2000) with presumed fluid Eu^{2+}/Eu^{3+} ratios of 0.4, 4, and 40. The model 3 of primary F-rich magmatic fluids is calculated based on the mean REE compositions of granitic melts (calculated by subtracting hypothetical proportions of 10%, 50%, and 80% REEs in crystallized accessory minerals from the granite porphyry) and the minimum liquid-liquid DFluoride/silicate REEs values from Veksler et al. (2012). The parameters and calculated results are listed in Supplementary Table S7.

Fig. 12. (a) $(La/Yb)_N$-δEu, (b) ΣREE (ppm)-Y (ppm), (c) Nb (ppm)-Ta (ppm), and (d) Mo (ppm)-Mn (ppm) binary diagrams of the Weijia scheelites.

Fig. 13. (a) ΣREE–Eu+Y (μmol/g) vs. Total Mg (apfu: atoms per formula unit) and (b) ΣREE–Eu+Y (μmol/g) vs. Total Al (apfu) correlational plots of the Weijia garnets. Legend refers to Fig. 10.

Fig. 14. (a) Nb+Ta (μmol/g) vs. ΣREE–Eu+Y (μmol/g), (b) Na (μmol/g) vs. ΣREE–Eu+Y (μmol/g), and (c) Nb+Ta+Na (μmol/g) vs. ΣREE–Eu+Y (μmol/g) correlational plots of the Weijia scheelites. Legend refers to Fig. 12.

Fig. 15. Rb/Sr vs. Mg/(Mg+Fe) diagram of the Weijia granite porphyry. These whole-rock geochemical data are from Zhao et al. (2016), Huang et al. (2017), and Wu et al. (2021).

Fig. 16. Eu_N vs. Eu* N $[(Sm_N \times Gd_N)^{1/2}]$ diagram (after Ghaderi et al., 1999) of the Weijia scheelites. Legend refers to Fig. 12.

Highlights

- Two stages of fluid exsolution are recognized in the Weijia W skarn deposit.
- F-rich magmatic fluids are enriched in REEs, Y, Nb, Ta with flat REE patterns.
- F consumption is critical for the compositional evolution of F-rich mineralizing fluids.
- Combined garnet and scheelite trace elements are powerful in tracking W skarn mineralization.